Quaternary Science Reviews 325 (2024) 108477

Contents lists available at ScienceDirect

Quaternary Science Reviews

journal homepage: www.elsevier.com/locate/quascirev

# Retreat patterns and dynamics of the former Norske Trough ice stream (NE Greenland): An integrated geomorphological and sedimentological approach

Adrián López-Quirós [a,b,*], Tuomas Junna [b], Joanna Davies [b], Katrine J. Andresen [c], Tove Nielsen [d], Negar Haghipour [e], Lukas Wacker [e], Aage Kristian Olsen Alstrup [f,g], Ole Lajord Munk [f,g], Tine L. Rasmussen [h], Christof Pearce [b], Marit-Solveig Seidenkrantz [b]

[a] Department of Stratigraphy and Paleontology, University of Granada, 18071, Granada, Spain
[b] Department of Geoscience, iCLIMATE Centre, and Arctic Research Centre, Aarhus University, 8000, Aarhus C, Denmark
[c] SeisLab Aarhus, Department of Geoscience, Aarhus University, 8000, Aarhus C, Denmark
[d] Geological Survey of Denmark and Greenland GEUS, 1350, Copenhagen K, Denmark
[e] Laboratory of Ion Beam Physics, ETH Zürich, Zürich, Switzerland
[f] Department of Nuclear Medicine & PET, Aarhus University Hospital, Aarhus, Denmark
[g] Department of Clinical Medicine, Aarhus University, Aarhus, Denmark
[h] Department of Geosciences, UiT the Arctic University of Norway, Tromsø, Norway

ARTICLE INFO

Handling Editor: Dr Giovanni Zanchetta

*Keywords:*
Submarine landforms
Sediment cores
Paleoceanography
LGM ice extent
Ice retreat
Holocene
Northeast Greenland

ABSTRACT

A better understanding of past extent and dynamics of the Greenland Ice Sheet (GrIS) is required to provide context for present-day observations, to constrain numerical climate models and to predict future scenarios of ice-sheet response to recent climatic change. The presence of a grounded GrIS on the NE Greenland shelf during the Last Glacial Maximum (LGM) is supported by high-resolution seismic data combined with multi-proxy analyses of sediment gravity cores from Norske Trough. Our results indicate that an ice stream advanced to the outer shelf during the LGM. Recessional moraines and grounding zone wedges on the seafloor of the outer to middle shelf show that initial retreat was episodic, punctuated by two major stillstands. Pinning points for grounding-zone stabilization were controlled by pre-LGM trough topography. In contrast, preserved large-scale glacial lineations on the seafloor of the inner shelf, formed during the advance, indicate that ice retreat from the inner trough to the coast-proximal position was rapid in order to maintain the former carved morphology. Initial ice retreat was underway before 16.6 cal Kyr BP, earlier than previously known for this sector of the NE Greenland shelf. The inner shelf was free from grounded ice at least by 12.5 cal Kyr BP, and likely before. Retreat occurred in a glaciomarine setting and the ice sheet was fringed by a floating ice shelf. There is no evidence of grounded-ice readvances during the Younger Dryas, although a floating ice shelf with vigorous sea-ice and iceberg rafting production occupied the inner shelf at 11.3 cal Kyr BP. $^{14}$C dates reveal initial stepwise ice retreat followed by a fast retreat that coincides with Heinrich Stadial 1 and the Bølling-Allerød interstadial, respectively. During both periods there was increased inflow of warm Atlantic Water, indicating a strong ocean/climate control on the late deglaciation of Norske Trough. Following the late deglaciation, postglacial (Holocene) sedimentation records a change from an ice-distal glaciomarine environment, to an open marine environment and complete ice shelf disintegration. On the innermost shelf of the Norske Trough, the ice shelf disintegrated and reformed once before the final break-up occurred at 9.6 cal Kyr BP.

## 1. Introduction

The Greenland Ice Sheet (GrIS) is the second largest ice sheet on Earth, storing ~7.4 m of potential global-mean sea-level rise equivalent (Bamber et al., 2013; Morlighem et al., 2017). In the last decades, the GrIS has contributed to global mean sea-level rise at a rate of 0.7

* Corresponding author. Department of Stratigraphy and Paleontology, University of Granada, 18071, Granada, Spain.
*E-mail address:* alquiros@ugr.es (A. López-Quirós).

https://doi.org/10.1016/j.quascirev.2023.108477
Received 7 June 2023; Received in revised form 11 December 2023; Accepted 17 December 2023

mm $yr^{-1}$ (Fürst et al., 2015; The IMBIE Team, 2020) as a result of runoff of surface meltwater and by ice discharge into the oceans (van den Broeke et al., 2016; Wood et al., 2021). The GrIS's contribution to global-mean sea-level rise during the 21st century is projected to increase in speed, albeit with a large uncertainty range (Shepherd et al., 2012; Church et al., 2013; Bamber et al., 2019). A significant feature of the GrIS is the NE Greenland Ice Stream (NEGIS; Joughin et al., 2001; Reeh et al., 2001), which comprises a ~600 km long ice stream that drains ~12% of the interior GrIS via fast-flowing, marine-terminating outlet glaciers: 79°-Glacier, Zachariae Isstrøm, and Storstrømmen (Khan et al., 2014; Mouginot et al., 2015) (Fig. 1A and B). NEGIS modeling investigations applying the different warming scenarios, outlined by the Intergovernmental Panel on Climate Change (IPCC), advocate that the Zachariae Isstrøm will rapidly retreat by up to 30 km upstream from its present-day location, adding ~16.2 mm to global-mean sea-level rise by 2100 (Choi et al., 2017). Accordingly, the ice stream will stabilize on a topographic ridge unless frontal summer melt rates exceed 6 m $day^{-1}$, which would possibly trigger a further inland retreat. This latter scenario is within the range of likely future scenarios stated by the IPCC (see IPCC, 2021).

The GrIS is known to have advanced to its furthest extent during the Last Glacial Maximum (LGM; ~20 kyr ago), providing a significant decrease in global sea-level at that time (e.g., Clark and Mix, 2002). Several studies of terrestrial glacial and related deposits have confirmed that ice advanced through the main fjord-systems of Greenland to reach at least the outer coastal areas at the LGM (e.g., Funder et al., 2011; Roberts et al., 2013). This consensus is sustained by numerical modeling of isostatic rebound from past ice-sheet loading; estimates are based on observations of dated raised beaches around coastal areas and offshore islands of Greenland (e.g., Fleming and Lambeck, 2004). It is less obvious, however, both where and how far the ice sheet may have extended across the broad continental shelf around Greenland, and what the nature of full glacial and deglacial ice-sheet dynamics may have been. In NE Greenland (~76–81°N; Fig. 1A), the extent of the ice margin during the LGM is particularly poorly constrained. Minimum estimations based only on a conceptual model, due to the lack of seismo-acoustic morphological investigations, suggest that the ice margin was located at the inner shelf (Funder et al., 2011, Fig. 1B). Conversely, more recent seismo-acoustic evidence from the shelf offshore of the NEGIS display a number of glacial seafloor features (submarine landforms), such as recessional moraines, grounding zone wedges and large-scale glacial lineations. Together, this suggests that the ice margin extended to the shelf edge (Evans et al., 2009; Winkelmann et al., 2010; Arndt et al., 2015, 2017; Olsen et al., 2020, Fig. 1B). This interpretation is reinforced by seismo-acoustic evidence of mass-wasting and turbidite flow deposits interpreted as glacially influenced sedimentary processes on the slope and deep basin offshore NE Greenland (e.g., Evans et al., 2009; García et al., 2012). However, recent studies indicate that the LGM ice sheet did not reach the shelf edge along the entire NE Greenland shelf (e.g., Spielhagen and Mackensen, 2021; Rasmussen et al., 2022). Moreover, the age of the submarine landforms is poorly constrained due to the absence of radiocarbon ($^{14}C$) dates from marine sediment archives in this regional setting. It is suggested that they were shaped during the LGM as they are not draped with a thick sediment cover (Arndt et al., 2017).

Radiocarbon ($^{14}C$) dates retrieved from the NE Greenland coastline adjacent to the present-day NEGIS show that deglaciation of this area likely occurred around 9.7–9.1 cal Kyr BP (Bennike and Björck, 2002), whereas a combination of $^{14}C$ and $^{10}Be$ ages indicate that the outer coast adjacent to the NE Greenland shelf was deglaciated by 11.7 ± 4 cal Kyr BP (Larsen et al., 2018) (Fig. 1A). This aligns with $^{14}C$ dates from glaciomarine deposits recovered close to the floating ice tongue of the 79°-Glacier on the inner NE Greenland shelf, indicative of postglacial marine conditions at least as early as 10.9 cal Kyr BP (Syring et al., 2020; Lloyd et al., 2023) (cores PS100/270 and PS100/198; Fig. 1A and B). In contrast, on the inner shelf of Norske Trough (90 km east of the NEGIS; Fig. 1B), Davies et al. (2022) evidenced that deglaciation in this area started at least as early as 12.5 cal Kyr BP, and likely prior to 13.4 cal Kyr BP. Other $^{14}C$ dates collected from the outer shelf of Westwind Trough reinforce deglacial conditions before 13.3 cal Kyr BP (Hansen et al.,

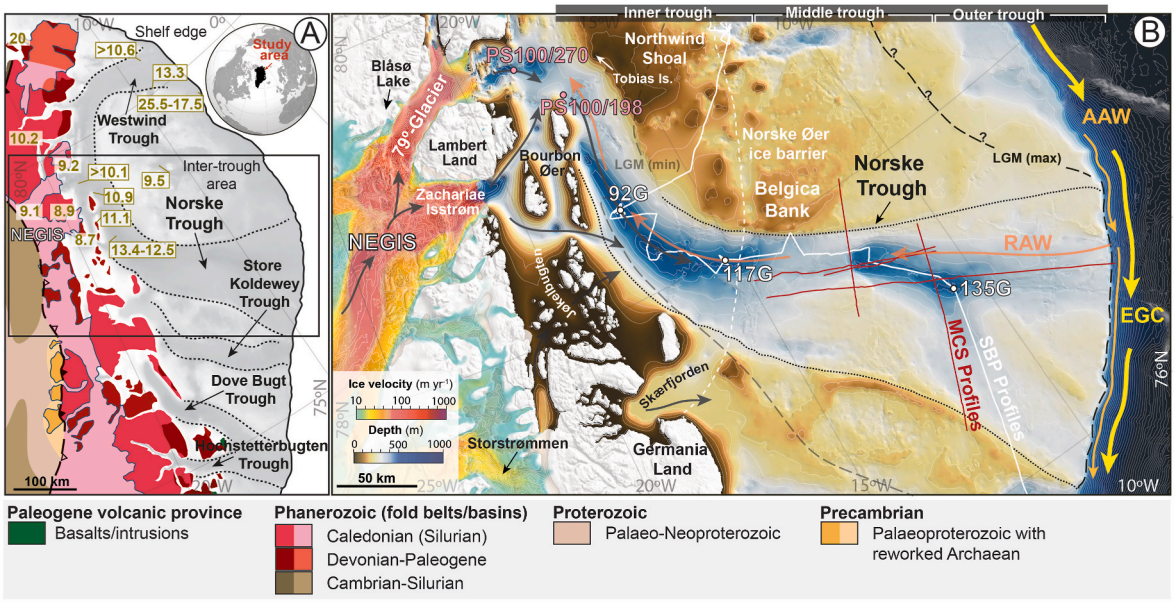


**Fig. 1.** A) Simplified lithostratigraphic map of NE Greenland (modified from Henriksen, 2003; Dawes, 2009). Timing of deglaciation on the NE Greenland continental shelf (in cal. Kyr BP) is also shown (from Bennike and Björck, 2002; Nørgaard-Pedersen et al., 2008; Larsen et al., 2018; Syring et al., 2020; Davies et al., 2022; Hansen et al., 2022; Rasmussen et al., 2022; Lloyd et al., 2023). B) Geographical setting of the study area showing the position of sub-bottom (SBP) and multichannel (MCS) seismic profiles and sediment cores involved in this study (white color). Ice velocities and major oceanographic currents are indicated. Inferred paleo-ice flow pathways (gray arrows; Arndt et al., 2015) and proposed minimum (LGM min; Funder et al., 2011) and maximum (LGM max; Evans et al., 2009; Arndt et al., 2017) last glacial maximum ice extents are also shown. Bathymetric map extracted from Arndt et al. (2015). Multiyear ice velocities (temporal coverage: December 1, 1995 to October 31, 2015) are from Joughin et al. (2018). EGC: East Greenland Current; AAW: Arctic Atlantic Water; RAW: Return Atlantic Water; NEGIS: Northeast Greenland Ice Stream.

2022, Fig. 1A). Further north at ~81°N (Independence Fjord system/-Wandel Sea), marine sediment cores indicate that deglaciation of the shelf here started as early as 20 cal Kyr BP (Nørgaard-Pedersen et al., 2008, Fig. 1A), while shelf areas further south at ~72–70°N (Kejser Franz Josef Fjord/Scoresby Sund) evidenced regional deglaciation by ~17–19 cal Kyr BP (e.g., Stein et al., 1996; Evans et al., 2002; Ó Cofaigh et al., 2004; Funder et al., 2011). Considering the vast area of this broad shallow shelf, the marine evidence from the fjords and the shelf of NE Greenland is very limited and the deglaciation history is very fragmented and thus remains uncertain.

This study is based on new data from an expedition to the NE Greenland shelf in 2017 (*NorthGreen 2017*; Seidenkrantz et al., 2018) that has yielded much new information on the extent, dynamics, and timing of late Quaternary ice-sheet behavior (e.g., Pados-Dibattista et al., 2022; Davies et al., 2022; Rasmussen et al., 2022; Jackson et al., 2022; Hansen et al., 2022). We here present new marine seismic, geochronological, and sedimentological data covering the largest glacial trough on the NE Greenland continental shelf, i.e., the 350 km-long and up to 200 km-wide Norske Trough (also known as Belgica Trough). The main objective of this study is to provide new knowledge about the maximum ice stream extent, influence of subglacial topography and the pattern and timing of ice retreat of this sector of the GrIS overlying Norske Trough during the LGM and the deglaciation. Accordingly, our observations and discussion encompass the post LGM ice retreat across the outer shelf of Norske Trough, to the area adjacent to the present margin of Bourbon Øer and Lambert Land, a major conjunction site of the two fast-flowing marine terminating outlet glaciers (i.e., 79°-Glacier and Zachariae Isstrøm) of the NEGIS (Fig. 1).

## 2. Regional setting

The study area is located on the NE Greenland shelf to the east of the NEGIS (Fig. 1). The large-scale, ~300 km wide, NE Greenland shelf is characterized by large cross-shelf troughs (Westwind, Norske/Belgica, Store Koldewey, Dove Bugt, and Hochstetterbugten troughs), separated by shallower inter-trough (banks/shoals) shelf areas (Arndt et al., 2015, Fig. 1A). The troughs are characteristic features of formerly glaciated continental shelves, interpreted as glacially over-deepened landforms acting as pathways for fast-flowing ice streams eroding into the subglacial bed (Batchelor and Dowdeswell, 2014, and references therein), while inter-trough shelf areas are interpreted to have been covered by slower flowing ice, experiencing less erosion (e.g., Ottesen and Dowdeswell, 2009; Klages et al., 2013). Onshore, the bedrock topography comprises Precambrian rocks, mostly Paleoproterozoic formations with reworked Archean crystalline rocks, overlain by undeformed Paleoproterozoic to Silurian sedimentary/volcanic rocks formed during the Caledonian Orogeny (e.g., Henriksen, 2003; Henriksen and Higgins, 2008; Dawes, 2009) (Fig. 1A). In addition, post-Caledonian sediments (mid-Devonian to Mesozoic) and lower Paleogene volcanic rocks are extensively exposed in the coastal areas (Fig. 1A; Henriksen, 2003; Dawes, 2009).

The study area is at present primarily influenced by the southward-flowing East Greenland Current (EGC), which carries cold, low-saline surface Polar Water (PW) and local meltwater from the GrIS (e.g., Johannessen, 1986; Bourke et al., 1987; Hopkins, 1991; Willcox et al., 2023). Below the PW, the water masses originate from Atlantic sources, i.e., from submerged and recirculated Atlantic-sourced waters from the Arctic (Arctic Atlantic Water: AAW; often referred as 'Arctic Intermediate Water') and from the 'warmer' Return Atlantic Water (RAW; often referred as 'Atlantic Intermediate Water') transported by the Return Atlantic Current (RAC) (Quadfasel et al., 1988; Rudels et al., 2005; de Steur et al., 2009; Schaffer et al., 2017; Gjelstrup et al., 2022). Due to the depth of the cross-shelf troughs in this area, they provide deep conduits for warmer Atlantic waters to reach marine terminating glaciers (Arndt et al., 2015); e.g., to the Zachariae Isstrøm glacier located at the western end of Norske Trough (Bentley et al., 2023) (Fig. 1B). An increased inflow of warmer Atlantic waters into NE Greenland cross-shelf troughs, and subsequently into fjords, is proposed to affect the submarine melt rates, causing instability at the grounding line of marine-terminating outlet glaciers (Khan et al., 2014; Mayer et al., 2018); e.g., the 79°-Glacier (Straneo and Heimbach, 2013; Wilson and Straneo, 2015) (Fig. 1B).

Norske Trough, here subdivided into an inner-, middle- and outer-trough (Fig. 1B), is a 350 km long, 35–200 km wide from inner to outer shelf, and up to 590 m deep. The NW-SE-oriented cross-shelf trough is located between ~79 and 76°N offshore NE Greenland (Fig. 1B). It is characterized by reverse bed slopes with its deepest section at the conjunction in front of 79°-Glacier and Zachariae Isstrøm (Arndt et al., 2015) (Fig. 1B). Arndt et al. (2017). This is identified by an assemblage of glacigenic submarine landforms in Norske Trough, including megascale glacial lineations and one grounding zone wedge (GZW). From the submarine landform assemblage, it was suggested that during the LGM, grounded ice advanced to the shelf edge, while during the Holocene deglaciation ice retreat was rapid, devoid of evidence for phases of grounding line stabilization, but of a later, possibly during the Younger Dryas (11.9–12.7 cal Kyr BP), ice readvance to a mid-shelf position (Arndt et al., 2017). However, $^{14}$C dates from glaciomarine deposits recovered on the inner Norske Trough (ST08-092G; Fig. 1B) established that postglacial marine conditions prevailed in this setting during most of the Younger Dryas (Davies et al., 2022).

## 3. Material and methods

This study is based on high-resolution seismic data and multi-proxy analysis of three gravity sediment cores (DA17-NG-ST12-135G, DA17-NG-ST10-117G, and DA17-NG-ST08-092G; hereafter 135G, 117G, and 92G; Fig. 1B) in a transect through Norske Trough. The integration of seismic data and core-based multi-proxy analysis has great potential to provide important information for paleoenvironmental reconstructions in glaciated continental margins and timing and patterns of ice retreat/advances (e.g., Nielsen and Rasmussen, 2018; Callard et al., 2020; Hogan et al., 2020; Olsen et al., 2020; López-Quirós et al., 2021). The high-resolution seismic dataset and sediment gravity cores were collected on board the RV *DANA* during the *NorthGreen2017* expedition (Seidenkrantz et al., 2018, Fig. 1B). Core 135G is 270 cm long and was collected at 500.9 m water depth at 77°7.648, 10°40.539′W; core 117G is 410 cm long and was obtained at 497.2 m water depth at 78°57.517, 15°26.966′W; core 92G is 585 cm long and was collected at 583 m water depth at 78°30.054′N, 16°16.711′W. Onboard, the cores were cut into 1-m sections and stored cold. At the Department of Geoscience, Aarhus University (Denmark), they were opened lengthwise and split into two halves (working and archive), and subsequently stored at 3 °C at the core repository. Non-destructive analyses (i.e., visual core description, X-ray fluorescence scanning, and computed tomography (CT); see below) were performed on the archive halves. Working halves were sampled for radiocarbon dating, sedimentological and/or mineralogical and micropaleontological analyses. Additionally, rumohr cores recovered at the same station as the gravity cores (DA17-NG-ST08-090 R, DA17-NG-ST10-109 R, and DA17-NG-ST12-134 R), and with intact and undisturbed sediment-water interface, were used to assess possible core-top losses during coring (gravity) operations (S. Fig. 1).

### 3.1. Seismic datasets

High-resolution singlechannel seismic data were acquired with an Innomar SES-2000 Deep Narrow-Beam Parametric Sub-Bottom Profiler. The subbottom profiler (SBP) data were acquired with a 4 kHz low-frequency pulse. The ping-rate was 0.97–1.70 pps (pings per sec.) within the 300–600 m water depth range, and up to ca. 3.6 pps for water depths around 150–200 m. SBP data was acquired both during transit between planned sampling stations and during dedicated surveys at these stations. Hence acquisition speed varied from 9 to 12 knots (during

transit) to around 4–6 knots during surveys. The frequency of 4 kHz gives a dominant pulse length of 37.5 cm, which assuming a sound velocity of 1500 m/s in the shallow sediments (Rebesco et al., 2011), provides a vertical resolution of ~19 cm (estimated as half the dominant pulse length). Moreover, the horizontal resolution (estimated by the width of the first Fresnel zone at water depths between 0.3 and 0.8 s of two-way travel time (TWT) was in the range of 12–21 m. As the motion sensor onboard the research vessel did not function during the North-Green2017 cruise, the collected signal was post-processed following standard processing (including heave-roll-pitch corrections) with RadExPro software, which solved most of the problem with the lacking heave-roll-pitch corrections during acquisitions. The resulting seismic data were then converted and imported as SEG-Y files into S&P Global Kingdom™ software for interpretation. About 500 km of SBP transects available for this study (Fig. 1B) provided new observations about the seismic stratigraphy of Norske Trough, where the SBP system could penetrate up to 80 m, assuming a conservative seismic velocity conversion of 1500 m/s for these shallow sub-seabed sediments (Rebesco et al., 2011). For the seismic-to-core tie, a sediment velocity of 1500 m/s was also used. Seismic unit thickness description is provided in seconds (s) of TWT. Isochore maps of seismic units identified in this work were constructed only for the total deglacial sediment pile, since this combined unit was recognized in a higher number of seismic profiles.

Commercial 2D multichannel seismic (MSC) reflection data crossing Norske Trough were made available by TGS-NOPEC Geophysical Company ASA. From these, selected profiles were used to correlate the seafloor reflection with SBP sections and to highlight the underlying control of deep geological structures on the morphology of recent sedimentary features (selected MCS profiles are shown in Fig. 1B). The MCS profiles have a dominant frequency around 140 Hz giving a dominant pulse length of 10 m and in turn a vertical resolution of about 5 m. Concerning morphosedimentary evolution, only the upper part of the MCS record, typically <1 s TWT, was studied in detail. This is considered sufficient to cover the glacier-influenced Pliocene and Pleistocene parts of the sedimentary record (Berger and Jokat, 2008, 2009; Newton et al., 2017). The quality of the MSC seismic profiles is variable, but mostly of good resolution.

### 3.2. Core chronology

A total of twenty-three new $^{14}$C radiocarbon dates were made by accelerator mass spectrometry (AMS) directly on gaseous samples (Wacker et al., 2013a, 2013b) for the chronology of cores 135G and 117G (Table 1). The age-depth model of core 92G is the same as presented by Davies et al. (2022) (S. Fig. 2A). The age-depth model of core 117G is based on eleven AMS $^{14}$C radiocarbon dates of mixed benthic and planktic foraminifera (eight and three samples, respectively; S. Fig. 2B). The age-depth model of core 135G is based on twelve AMS $^{14}$C radiocarbon dates of mixed benthic and planktic foraminifera (eight and four samples, respectively; S. Fig. 2C). Samples containing >50 μg carbon (core 92G; Davies et al., 2022) and between 24 and 49 μg carbon (core 135G) were leached with diluted HCl (e.g., see Bard et al., 2015) prior to the analysis (Table 1). The measured leach fractions were consistently in good agreement with the corresponding main fractions, confirming that samples from these cores were clean and homogeneous. However, some samples were very small and could not be leached. The AMS $^{14}$C dating was performed at the Laboratory of Ion Beam Physics at ETH Zürich (Switzerland) and all $^{14}$C ages were calibrated using CALIB Radiocarbon Calibration Program 8.2 (Stuiver et al., 2021) and the MARINE20 calibration curve (Heaton et al., 2020) (Table 1). As proposed for this region in previous studies (e.g., Håkansson, 1973; Funder, 1982; Davies et al., 2022) and based on the Marine Reservoir Correction Database (Reimer and Reimer, 2001), we have considered a local marine reservoir age correction (ΔR) of 1 ± 32 years in all samples (Table 1).

### 3.3. Sedimentological analysis

Sedimentary units were defined on the basis of visual core descriptions and sediment composition analysis (Tucker, 2001). Textural classification of Folk (1954) was applied. Sediment characterization included lithology, sediment texture and structure, sediment color using the Munsell color chart, bioturbation intensity and grain size.

Macroscopic visual core observations were aided by (a) high-resolution line scan digital images and 2D high-resolution X-radiographic images obtained from archive halves using an ITRAX X-ray fluorescence (XRF) core scanner (Cox Analytical) at the Department of Geoscience, Aarhus University (Denmark), and (b) computed tomography (CT) images obtained from archive halves using a Siemens Biograph Vision 600 medical PET/CT scanner at the Department of Nuclear medicine & PET, Aarhus University Hospital (Denmark). X-radiograph analysis (voltage: 60 kV; current: 45 mA; exposure time: 2000 ms) were conducted at 100 μm-interval resolution in a narrow (2 cm) track along the long-axis (center) of surface core sections. CT scan parameters for cores 135G and 117G were: 120 kV, 300 Eff mAs, 200 mm field of view, slice thickness 0.6 mm, filter Br60, whereas details about the CT scan of core 92G can be found in Davies et al. (2022). The resulting CT images (~1800 images per section) were then imported into the image editing software FIJI (ImageJ; Rueden et al., 2017) and the mean Hounsfield units (HU) value extracted to calculate sediment density (Reilly et al., 2017).

Bulk grain-size distribution was measured for cores 135G and 117G using a laser diffraction particle sizer (Sympatec HELOS) at the Department of Geoscience, Aarhus University (Denmark). Bulk grain-size distribution for core 92G is from Davies et al. (2022). In addition, the relative composition of terrigenous and biogenic grains and grain size and shape were examined microscopically in core 117G, using a digital microscope (DeltaPix) and a field emission scanning electron microscope (FESEM). During the petrographic grain composition study, several images were taken with an Invenio 6EIII – 6.3 MP camera connected to a 3D Digital Microscope (DeltaPix) and captured with the InSight image-management software at the Department of Geoscience, Aarhus University (Denmark). Secondary electron (SE) and back-scattered electron (BSE) imaging were obtained with a GEMINI (FESEM) CARL ZEISS microscope at the Scientific Instrumentation Center, University of Granada (Spain), equipped with an energy-dispersive X-ray spectroscopy system (EDX). Concentration of clasts indicative of ice-rafted debris (IRD) was quantified by counting the >2 mm clasts on CT images for cores 135G and 117G (Grobe, 1987; Jennings et al., 2002). Clasts were counted within a 2 × 10 cm window at 5 cm resolution using the image editing software FIJI. Clasts (>3 mm) per 12 cm diameter core slice were counted at 2 cm resolution in core 92G (Davies et al., 2022). Additionally, concentration of clasts per gram of dry sediment was counted in core 117G at 10 cm resolution following standard methods of Bond and Lotti (1995) and Krissek (1995). Clast counts were achieved on the 250–2000 μm fraction using a binocular microscope, while petrographic grain composition was stablished by using the subsequent groups: (a) crystalline rocks, quartz and feldspar; (b) metamorphic and volcanic rocks, and olivine grains, mica and glass shards; (c) clastic sedimentary rocks; and (d) carbonate sedimentary rocks. This was done for comparison with the counted CT images, which reproduce similar bottom-up trends.

A detailed analysis of the foraminiferal assemblages in core 92G has previously been performed by Davies et al. (2022). For cores 117G and 135G we here only calculated the foraminiferal concentrations at selected intervals within each sedimentary unit. For each of these samples, the sediment was washed through sieves of mesh diameters of 0.1 and 1.0 mm and the dried 0.1–1.0 mm fraction was investigated for the presence of foraminifera.

**Table 1**
Radiocarbon dates from sediment cores DA17-NG-ST08-092G, DA17-NG-ST10-117G, and DA17-NG-ST12-135G. Dates from core 92G are from Davies et al. (2022). The CALIB 8.1.0 software (Stuiver et al., 2021) and the MARINE20 dataset (Heaton et al., 2020) were used to convert the $^{14}$C ages to calendar ages with 2σ precision, applying a local marine reservoir age correction (ΔR) of 1 ± 32 years following Håkansson (1973), Funder, 1982 and Davies et al. (2022). Samples marked with (#) contained >50 μg carbon (core 92G) and between 24 and 49 μg carbon (core 135G). These samples were leached for quality control (e.g., Bard et al., 2015), while the rest of the samples were very small and could not be leached. Samples marked with (*) were ultra-small (<10 μg) to be considered realistic in this study. Note that the numbers in bold are the radiocarbon dates shown in the stratigraphic log/correlation of sediment cores (92G, 117G, and 135G) presented in Fig. 7.

| Core depth (cm) | Lab ID (ETH) | Material | Uncorrected age ($^{14}$C yr BP) | Error (±yr) | Unmodelled calibrated age range (2σ) (cal. Yr BP) | | | Source |
|---|---|---|---|---|---|---|---|---|
| | | | | | Lower. Cal. Range | Upper. Cal. Range | Modelled median age | |
| **DA17-NG-ST08–092G** | | | | | | | | |
| 0.5 | 113,890 (#) | *Mixed planktonic foraminifera* | 595 | 50 | 528 | 657 | **597** | Davies et al. (2022) |
| 60.5 | 110,857 (#) | *Mixed planktonic foraminifera* | 7130 | 60 | 7793 | 8156 | **7946** | Davies et al. (2022) |
| 90.5 | 110,859 (#) | *Mixed planktonic foraminifera* | 7865 | 60 | 8540 | 8984 | **8670** | Davies et al. (2022) |
| 130.5 | 110,860 (#) | *Mixed planktonic foraminifera* | 8505 | 70 | 9310 | 9658 | **9495** | Davies et al. (2022) |
| 186.5 | 95,393 | *Mixed benthic foraminifera* | 8855 | 70 | 9687 | 10,189 | **9919** | Davies et al. (2022) |
| 240.5 | 110,862 | *Mixed planktonic foraminifera* | 9090 | 70 | 9967 | 10,496 | **10,284** | Davies et al. (2022) |
| 320.5 | 110,865 | *Mixed planktonic foraminifera* | 9400 | 70 | 10,410 | 11,067 | **10,748** | Davies et al. (2022) |
| 340.5 | 95,394 | *Mixed benthic foraminifera* | 9710 | 80 | 10,773 | 11,255 | **11,043** | Davies et al. (2022) |
| 406 | 113,885 | *Mixed benthic foraminifera* | 10,080 | 120 | 11,240 | 12,425 | **11,640** | Davies et al. (2022) |
| 451.5 | 113,886 | *Mixed benthic foraminifera* | 10,180 | 120 | 11,336 | 12,466 | **12,074** | Davies et al. (2022) |
| 452.5 | 113,889 | *Shell fragment* | 10,220 | 130 | 11,355 | 12,480 | **12,062** | Davies et al. (2022) |
| 464.5 | 95,395 | *Mixed benthic foraminifera* | 10,490 | 270 | 12,099 | 12,688 | **12,261** | Davies et al. (2022) |
| 486.5 | 113,888 | *Mixed benthic foraminifera* | 10,200 | 190 | 11,268 | 12,595 | **12,473** | Davies et al. (2022) |

| **Core depth (cm)** | **Lab ID (ETH)** | **Material** | **Uncorrected age ($^{14}$C yr BP)** | **Error (± yr)** | **Corrected and calibrated age (2σ) (cal. Yr BP)** | | | **Source** |
|---|---|---|---|---|---|---|---|---|
| | | | | | Lower. Cal. Range | Upper. Cal. Range | Median probability | |
| **DA17-NG-ST10–117G** | | | | | | | | |
| 68 | 121069.1.1 | *Mixed planktonic foraminifera* | 5920 | 70 | 5915 | 6335 | 6138 | This study |
| 68 | 121068.1.1 | *Mixed benthic foraminifera* | 6765 | 70 | 6841 | 7283 | **7071** | This study |
| 88 | 121070.1.1 | *Mixed benthic foraminifera* | 8310 | 90 | 8399 | 8960 | **8660** | This study |
| 98 | 121072.1.1 | *Mixed planktonic foraminifera* | 9315 | 80 | 9632 | 10,196 | 9937 | This study |
| 98 | 121071.1.1 | *Mixed benthic foraminifera* | 9400 | 90 | 9704 | 10,327 | **10,043** | This study |
| 108 | 121073.1.1 | *Mixed benthic foraminifera* | 10,275 | 80 | 10,998 | 11,593 | **11,256** | This study |
| 125 | 121075.1.1 | *Mixed planktonic foraminifera* | 10,070 | 100 | 10,624 | 11,248 | 10,962 | This study |
| 125 | 121074.1.1 | *Mixed benthic foraminifera* | 10,500 | 130 | 11,173 | 12,000 | **11,571** | This study |
| 140 | 127733.1.1 (*) | *Mixed benthic foraminifera* | 19,120 | 480 | 20,937 | 23,228 | 22,160 | This study |
| 272 | 127734.1.1 (*) | *Mixed benthic foraminifera* | 10,230 | 290 | 10,334 | 12,072 | 11,200 | This study |
| 329 | 127735.1.1 (*) | *Mixed benthic foraminifera* | 8570 | 310 | 8212 | 9764 | 8990 | This study |
| **DA17-NG-ST12–135G** | | | | | | | | |
| 65 | 126101.1.1 | *Mixed benthic foraminifera* | 2655 | 90 | 1891 | 2453 | **2175** | This study |
| 90 | 121065.1.1 | *Mixed planktonic foraminifera* | 8760 | 120 | 8912 | 9532 | **9237** | This study |
| 100 | 121080.1.1 (#) | *Mixed planktonic foraminifera* | 8975 | 80 | 9246 | 9760 | 9486 | This study |
| 100 | 121054.1.1 (#) | *Mixed benthic foraminifera* | 8915 | 90 | 9132 | 9676 | **9417** | This study |
| 120 | 121066.1.1 (#) | *Mixed planktonic foraminifera* | 10,840 | 80 | 11,799 | 12,443 | 12,107 | This study |
| 120 | 121055.1.1 (#) | *Mixed benthic foraminifera* | 11,575 | 90 | 12,695 | 13,111 | **12,900** | This study |
| 140 | 121067.1.1 (#) | *Mixed planktonic foraminifera* | 13,470 | 120 | 15,012 | 15,772 | 15,389 | This study |
| 140 | 121056.1.1 (#) | *Mixed benthic foraminifera* | 13,400 | 100 | 14,968 | 15,638 | **15,299** | This study |
| 170 | 121064.1.1 | *Mixed benthic foraminifera* | 14,070 | 130 | 15,756 | 16,584 | **16,172** | This study |
| 210 | 121063.1.1 | *Mixed benthic foraminifera* | 14,450 | 220 | 16,059 | 17,240 | **16,652** | This study |
| 222 | 126102.1.1 (*) | *Mixed benthic foraminifera* | 24,840 | 650 | 26,963 | 29,590 | **28,194** | This study |
| 274 | 126103.1.1 | *Mixed benthic foraminifera* | >41,000 | | 43,088 | | | This study |

### 3.4. Geochemical and physical properties

Elemental concentrations were measured on core surfaces of the archive halves at 0.2-mm interval resolution, using an ITRAX X-ray fluorescence (XRF) core scanner (Cox Analytical) at the Department of Geoscience, Aarhus University (Denmark). All core sections were scanned using a molybdenum tube (step size: 0.2 mm; exposure time: 10 s; voltage: 30 kV, current: 30 mA). The results of the XRF scanning are provided as element intensities in total counts per second (cps), which are relative to the real chemical concentration of the measured elements (Weltje and Tjallingii, 2008). More detailed information about the underlying principles and operation of the ITRAX core scanner is available in Croudace et al. (2006). Magnetic susceptibility (MS) was measured at 5-mm interval resolution using a Bartington MS2 fitted within the ITRAX core scanner. The measured MS is a volume magnetic susceptibility k with units of $10^{-5}$ SI and precision up to $2 \times 10^{-6}$ SI. For the present study, besides MS profiles, we only report on the following elements and elemental ratios: Manganese (Mn), Titanium (Ti), Aluminum (Al), Iron (Fe), Silica (Si), Potassium (K), Calcium (Ca), Strontium (Sr), and Barium (Ba), as well as the ratios Fe/K, K/Ti, Fe/Ca, Ca/Sr and Ca/K. Elemental counts of Ti, Si, K, and Al, commonly used as proxies for terrestrial detrital input (e.g., Rothwell and Croudace, 2015; Salabarnada et al., 2018; Evangelinos et al., 2020; López-Quirós et al., 2021), have been plotted against lithological logs to assess variations in the influx of terrigenous materials to the study area. Elemental counts of Fe have been similarly used as tracers of the influx of terrigenous materials (Rothwell and Croudace, 2015), though in combination with elemental counts of Mn, they have been used as indicators of paleo-oxidation fronts (e.g., Richter et al., 2006; Wolters et al., 2010). Elemental counts of Ca and Sr have been strictly used as tracers of biogenic origin among others (Zaragosi et al., 2006; Rothwell and Croudace, 2015). Elemental counts of Ba are reported as sensitive indicators of export paleoproductivity (Röhl et al., 2007; Ziegler et al., 2010). K/Ti ratios are sensitive to glacial/interglacial fluctuations (Bertram et al., 2018), as variations in K/Ti ratios indicate the source of detrital particles (e.g., Monien et al., 2012; Bertram et al., 2018) and are related with the amount of mica and illite phyllosilicates present (Diekmann et al., 2008). Ca/K ratios have been reported as tracers of biogenic carbonate vs. illite variations (Hebbeln et al., 2006). Other ratios have been previously used as proxies of terrigenous vs. biogenic $CaCO_3$ sedimentation (e.g., Fe/Ca ratios, Rogerson et al., 2006; Rothwell and Croudace, 2015). Furthermore, more specific interpretations concerning detrital composition have been used (e.g., Fe/K rations indicate changes in terrigenous mineralogy, Blanchet et al., 2009; while Ca/Sr ratios are used for detection of detrital carbonate deposition, Hodell et al., 2008). In addition to element concentration measurements, measurements of molybdenum (Mo) incoherent and coherent scattering were provided during XRF core scanning. The incoherent/coherent scattering ratio (inc/coh) is dependent on the average atomic number of materials in the sediment; organic carbon has a lower average atomic mass than silica or aluminosilicate and carbonate minerals. This ratio thus increases with greater organic carbon concentrations and has been previously used as an indicator of organic matter content (e.g., Sáez et al., 2009; Chawchai et al., 2016).

Shear strength measurements (undrained, KPa) were determined at selected sediment core intervals of cores 135G and 117G with a hand-held CONTROLS shear vane.

## 4. Results and interpretation

In this section, the description and interpretation of seismic datasets (MCS and SBP transects; Sections 4.1., 4.2. and 4.3.) are followed by analysis of sediment cores and their interpretation in terms of depositional processes (Sections 4.4. and 4.5.).

### 4.1. Seismic stratigraphic framework of Norske trough

Two major seismic sequences (Seq-1 and Seq-2), bounded at the top by the seabed and below by a pronounced erosional escarpment, are defined from the MCS data based on stratal stacking patterns and seismic reflection terminations (Fig. 2). A distinct, angular unconformity divides the sequences into an underlying, mainly aggrading sequence (Seq-1) and an overlying, eastward prograding 'wedge' sequence (Seq-2) (Fig. 2B).

Observed stacking patterns and seismic reflection terminations in Norske Trough, as previously interpreted in other NE Greenland shelf domains (e.g., see Døssing et al., 2016; Petersen, 2021), indicate a prominent eastward shelf progradation along the trough, with the older Seq-1 displaying a marked tectonic influence on their stacking patterns (changing dips of the clinoforms and internal deformation; Fig. 2B and C). In contrast, Seq-2 shows a normal regressive stacking pattern (Fig. 2B), which is consistent with a passive infill of the margin (Berger and Jokat, 2008, 2009). Seq-2 is interpreted as a prograding wedge and is further sub-divided in seq-2a and seq-2b (Fig. 2B). The sequence ages are poorly constrained due to the lack of longer sediment coring data from the NE Greenland shelf. However, tentative ages are suggested based on close-by available seismic-to-borehole ties at ODP-sites 909 and 913 (see Hull et al., 1996; Hamann et al., 2005; Berger and Jokat, 2008, 2009): Seq-1 is attributed to an upper Eocene to mid-Miocene age, whereas Seq-2 is attributed to a mid-Miocene to Recent age. Accordingly, the seismic unconformity (referred by Døssing et al., 2016 as intra-Miocene unconformity, 'IMU reflection'; e.g., Fig. 2B) is attributed to a middle to late Miocene (~15-10 Ma) age. Thus, seq-2a is attributed to mid-Miocene to end-Pliocene age, while seq-2b corresponds to post-Pliocene to Recent age (Fig. 2B).

Concerning morphosedimentary evolution, the upper part of the studied MCS sections show a present-day morphology guided by the underlying, glacier-influenced bed topography (Fig. 2B–F). For example, we interpret the observed mid-shelf seafloor wedge-shaped depositional systems 'GZW-2' (see Section 4.2) to have formed due to a prominent topographic high (buried, pre-LGM, possibly GZW) in the underlying bed topography (Fig. 2B–D). According to Batchelor and Dowdeswell (2015), the favored formation of GZWs at topographic highs in cross-shelf troughs may lead to the repeated placement of grounding-zone lines and the establishment of complex GZWs. In high-latitude cross-shelf troughs, a large number of GZWs occur in relation with underlying topographic highs that have been suggested to act as pinning points for grounding ice stabilization during retreat (e.g., Joughin et al., 2004; Ottesen et al., 2007; Dowdeswell and Fugelli, 2012; Batchelor and Dowdeswell, 2015; Newton et al., 2017; Nielsen and Rasmussen, 2018). Therefore, the pre-existing glacier-influenced bed topography in Norske Trough could have provided pinning points for grounding-zone stabilization during retreat (see below).

### 4.2. Shallow seismic facies and stratigraphic units

Within the upper part of Seq-2b, three major seismic facies are distinguished based on the seismo-acoustic characterization using the SBP data. The seismic facies are: (I) non-penetrative, (II) stratified, and (III) transparent seismic facies. The description, interpretation and distribution of seismic facies are shown in Fig. 3A. Based on these seismic facies, we have defined two seismic stratigraphic units (SU-1 and SU-2) from the SBP data (Fig. 3B, C, D).

SU-2, the lower seismic stratigraphic unit, is structureless and characterized by an irregular but relatively flat bottom reflection with medium to high amplitude (Refl-b; Fig. 3B and C). The unit has an acoustically semi-transparent to transparent signature (seismic facies III) and an irregular top reflection with high amplitude and continuity (Refl-a; Fig. 3B and C). In places, SU-2 shows a distinct mounded morphology (e.g., Fig. 3B) defining trough-parallel grooves and ridges. Where mounded, SU-2 reaches thicknesses of up to 25 m, and the

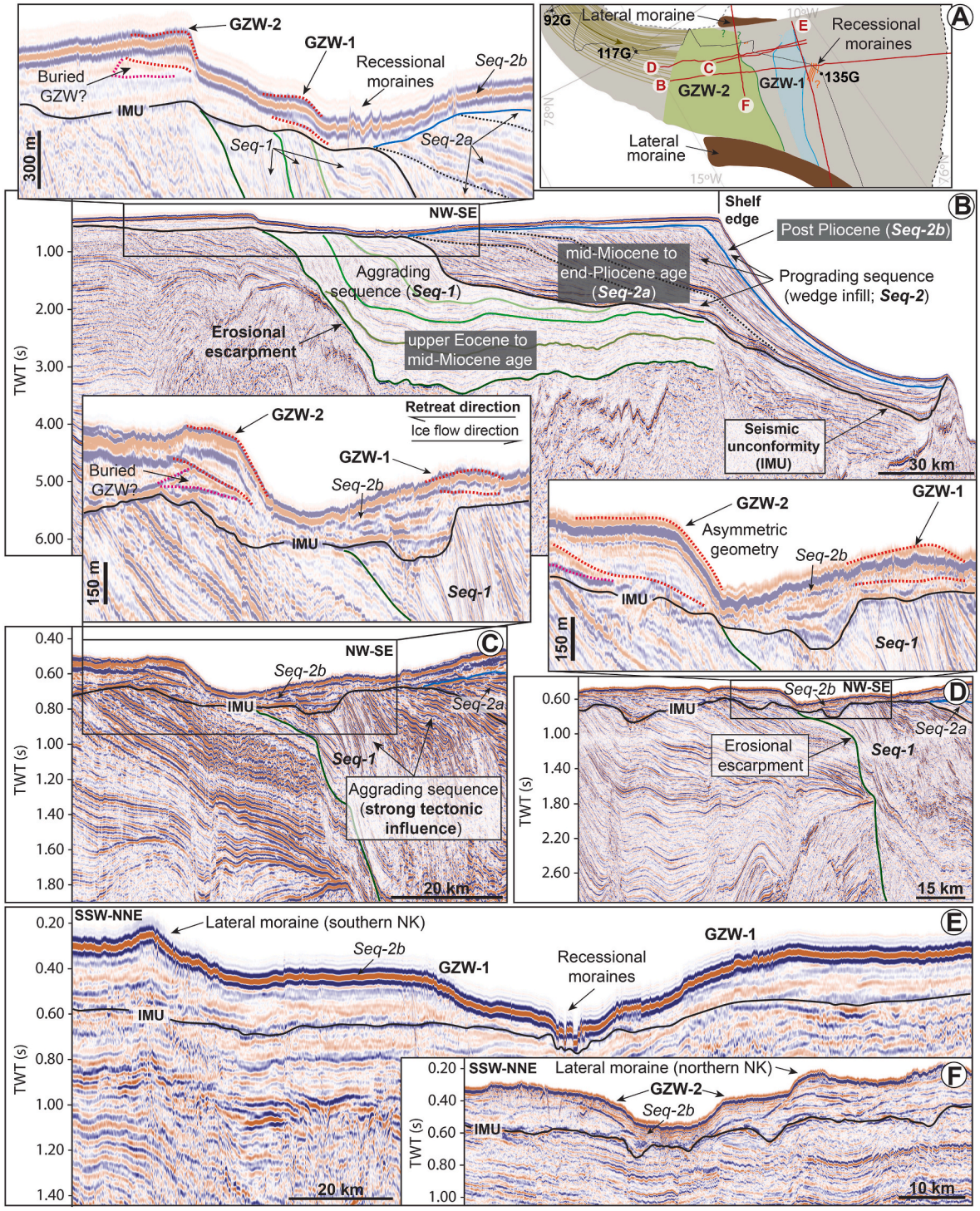


**Fig. 2.** Seismic stratigraphic framework of Norske Trough. A) Location of multichannel seismic (MCS) profiles (in red) and mapped glacial seafloor features. For complete information, see morphological map in Fig. 4. B) MCS profile showing significant regional tectonic and stratigraphic structures. Two major seismic sequences (Seq-1 (below) and Seq-2 (above)) separated by an angular intra-Miocene unconformity (IMU reflection; Døssing et al., 2016), and bounded below by a pronounced erosional escarpment, is identified. The Seq-2 sequence was further sub-divided in a lower seq-2a and upper seq-2b. Enlarged squared area show detailed morphosedimentary features based on the upper part of the MCS record (e.g., GZWs and moraines). Note that a buried, pre-LGM, pre-existing topographic high (possibly a GZW) is observed below an important surface GZW (GZW-2). C) and D) Detailed surface/buried pre-existing topographic highs (possibly GZWs) observed above IMU reflection (see enlarged square areas). E) and F) Examples of other observed glacial seafloor features (e.g., lateral and recessional moraines).

individual ridges have widths of 120–900 m and reliefs between 5 and 15 m. Their lengths likely cover several tens of kilometres.

The structureless and acoustically transparent nature of SU-2 is interpreted as subglacial till, comparable to the acoustic signature reported from other cross-shelf troughs on high-latitude glaciated margins (Dowdeswell et al., 2004; Evans et al., 2009; Ó Cofaigh et al., 2005, 2007). The structureless nature may also indicate that the till has a massive structure (Evans et al., 2009). In addition, the mounded morphology of SU-2 is interpreted as glacial lineations (see below) based on its similarity to comparable landforms reported from other cross-shelf

troughs, both in Greenland and Antarctica (e.g., Ó Cofaigh et al., 2005; Evans et al., 2009; Arndt et al., 2017). The presence of glacial lineations on SU-2, which form subglacially (e.g., Ó Cofaigh et al., 2005), provides further constraints for a subglacial till interpretation. Furthermore, SU-2 correlates with massive, matrix-supported soft diamicton in cores 135G and 117G, interpreted as subglacial basal till (i.e., lithological unit VII; see below).

SU-1 is acoustically stratified (seismic facies II) in most of the inner trough (Fig. 3B and C), while it shows semi-transparent to transparent reflections (seismic facies I) in the outermost inner to middle and outer trough (Fig. 3C). SU-1 is up to 37 m thick and occurs locally, either as basin infill or as draping above the underlying mounded SU-2 unit in the inner trough (Fig. 3D). In the innermost trough, unit SU-1 is further subdivided by reflection Refl-a' (Fig. 3B and C), which marks the transition from an upper low-amplitude stratified succession (SU-1a) to a lower high-amplitude stratified succession (SU-1b). In some places, SU-1b further comprises thin layers with a transparent to low-amplitude acoustic signature.

Based on its stratification/infilling geometry, SU-1 is interpreted as a product of glaciomarine/hemipelagic sediment deposition during and after ice stream retreat. Similar acoustic signatures have been reported in other glaciated margins, and their formation is interpreted as a product of glaciomarine suspension settling and/or turbidity and bottom current deposition (e.g., Ó Cofaigh and Dowdeswell, 2001; Dowdeswell et al., 2004; Ó Cofaigh et al., 2005; Hogan et al., 2012; López-Quirós et al., 2021). In addition, the low-amplitude layers internally of SU-1b (Fig. 3B) may be indicative of a diamictic-like composition, the genesis of which may be related to debris flow activity (Hogan et al., 2012; Callard et al., 2020). This suggests that SU-1b is composed of interbedded suspension settling and debris-flow deposits. Furthermore, SU-1 is correlated with interpreted proglacial and distal glaciomarine sediments in cores 135G, 117G and 92G (i.e., lithological units VI to I; see below). Accordingly, SU-1 is interpreted to reflect a gradual transition from ice-proximal to distal environments.

### 4.3. Seabed geomorphology: submarine landforms

The SBP dataset from Norske Trough reveals glacial features

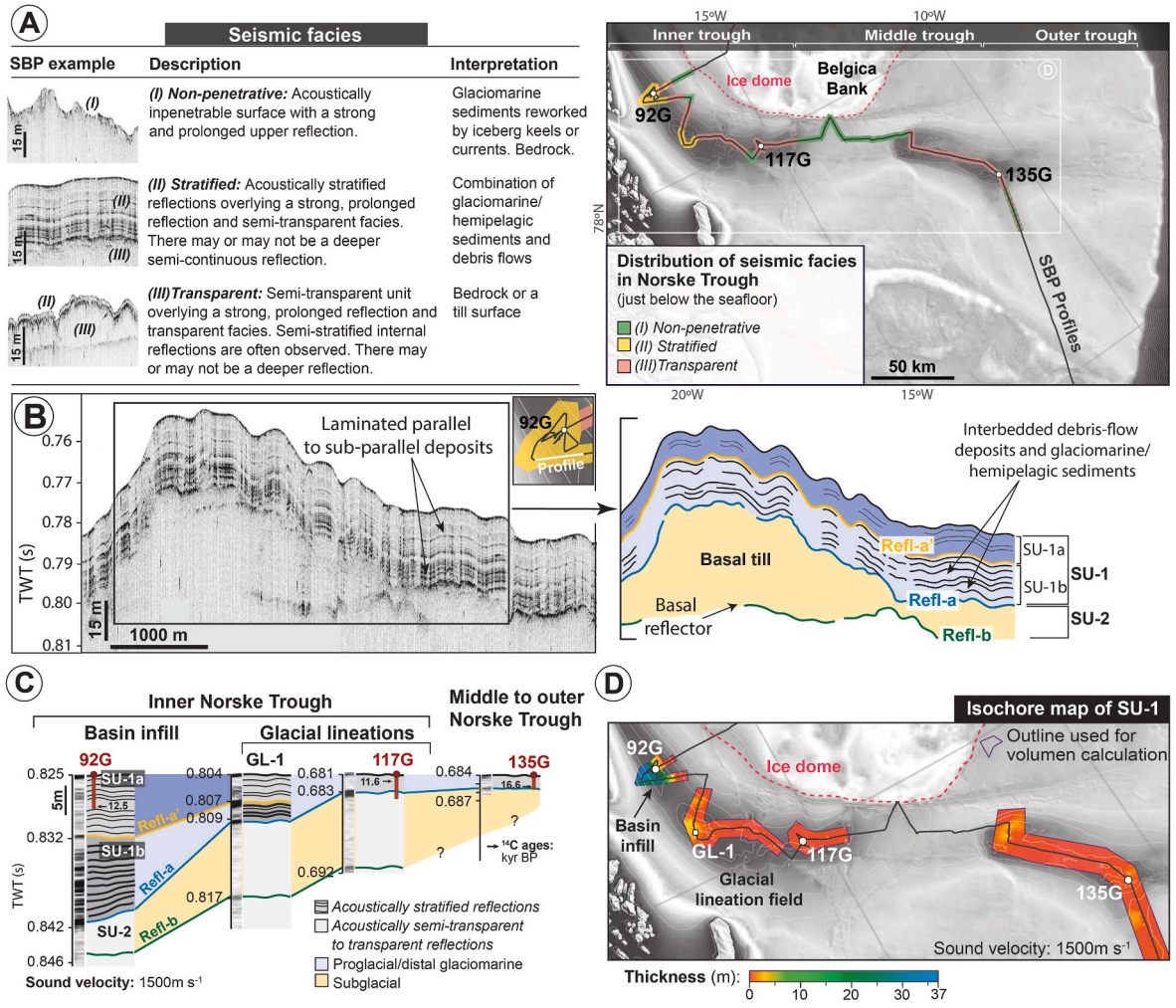


**Fig. 3.** Acoustic characterization, seismic stratigraphy and deglacial (SU-1) sediment volumes in Norske Trough for the upper part of Seq-2b. A) Identified acoustic seismic facies and corresponding facies distribution map. B) Defined seismic stratigraphic units. Example of an uninterpreted and interpreted SBP section displaying the two main seismic stratigraphic units (SU-1 and SU-2). In the innermost trough, unit SU-1 is further subdivided by Refl-a' in SU-1b and SU-1a. Profile location in the inset map. C) High resolution seismic stratigraphy across Norske Trough plotted vs. two-way travel time (TWT). Two main seismic discontinuities (reflections Refl-b and Refl-a) were identified as the base of the subglacial (SU-2) and proglacial to distal glaciomarine (SU-1) sedimentation. A third reflector (Refl-a') was recognized in the inner trough, delimiting SU-1b (glaciomarine/hemipelagic with interbedded debris-flow deposits) and SU-1a (glaciomarine/hemipelagic). The location and penetration of sediment cores DA17-NG-ST08-092G, DA17-NG-ST10-117G and DA17-NG-ST12-135G are marked in dark red. Radiocarbon dates for the cores are shown next to the cores. D) Isopach map of the deglacial sediment pile: SU-1b + SU-1a (using a sound velocity of 1500 m/s). Outline used for volume calculation is indicated in orange.

interpreted to reflect patterns of ice stream dynamics during the last deglaciation (Fig. 4).

#### 4.3.1. Glacial lineations

The streamlined, trough-parallel grooves and ridges of SU-2 occur principally in the inner trough, terminating close to a major wedge-shaped depositional system (GZW-2; Figs. 4 and 5). All of these parallel to sub-parallel linear ridges are aligned with the centerline of the trough (Fig. 4). Sparse subtle linear ridges have previously been reported at the shelf edge (Arndt et al., 2017, Fig. 4).

Based on the spatial distribution, dimensions and orientation, the trough-parallel grooves and ridges are interpreted as glacial lineations, formed subglacially by deformation of a low shear strength basal till layer (SU-2) at the base of a fast-flowing grounded ice stream advance (e.g., Dowdeswell et al., 2004; King et al., 2009; Spagnolo et al., 2014; Batchelor and Dowdeswell, 2015). Similar streamlined features have been reported on the seafloor of other formerly glaciated continental margins; here they have been interpreted to indicate the presence of grounded ice streams (Canals et al., 2000; Evans et al., 2009; Rydningen et al., 2013; Andreassen et al., 2014; Hogan et al., 2016; Arndt et al., 2017; Arndt, 2018).

#### 4.3.2. Grounding-zone wedges (GZWs)

Two asymmetrical wedge-shaped depositional systems are present within the outer to middle trough (GZW-1 and GZW-2; Figs. 2, 4 and 6). GZW-2 was originally mapped by Arndt et al. (2015). The GZWs, spaced 25 km from each other, are ~30–50 m high and several kms wide (Figs. 2, 4 and 6). The two GZWs are observed within and otherwise acoustically semi-transparent to chaotic unit (seismic facies I) (Fig. 6). The base of the two wedge-shaped depositional systems is unfortunately impossible to recognize on our SBP sections (Fig. 6D and E). However, on the MCS data, the two GZWs are linked to a thick, ~180 m sedimentary succession that occurs above dipping reflections (Seq-1) on the prograding shelf of Norske Trough (Fig. 2). This observation rules out that these features are bedrock sills.

Based on the seismo-acoustic morphological characterization, the wedge-shaped depositional systems are interpreted as grounding-zone wedges (GZWs) recording the position of the grounding line during temporary stillstands (i.e., the relatively long-lasting halts during the overall retreat; Dowdeswell et al., 2008; Batchelor and Dowdeswell, 2015). In our data, the observed GZWs are found superimposed on the glacial lineations (at their base, Figs. 4 and 6B), providing evidence that they were formed during a recessional trend. GZWs are more likely to form in regions where the vertical accommodation space beyond the grounding-zone is limited by the presence of floating ice shelves (e.g., Batchelor and Dowdeswell, 2015, and references therein). Thus, the establishment of floating ice shelves in the study area most likely contributed to the formation of GZWs. Moreover, the transparent character of these wedge-shaped depositional systems (Fig. 6E) indicates that the GZWs most likely formed by the deposition of unconsolidated, water-saturated subglacial till during such temporary stillstands as reported in comparable settings (e.g., Ó Cofaigh and Stokes, 2008; Rebesco et al., 2011).

#### 4.3.3. Recessional moraines

A number of likely low-relief, transverse and/or semitransverse ridges, with a low-amplitude to transparent seismic facies (seismic facies I; Fig. 6D and E), are documented on the seafloor of the middle to outer trough (Figs. 2, 4 and 6). The ridges are up to 1250 m wide, have reliefs <45 m and have a spacing of ~100–600 m (e.g., enlarged area in Fig. 6E). The ridges were predominantly mapped in the outer trough, further east of GZW-1, while small ridges are also present between GZW-1 and GZW-2 (Figs. 4 and 6D). Our limited available seismic data coverage does, unfortunately, not allow a further description of the ridges' shape, orientation and spatial distribution.

Based on the seismo-acoustic morphological characterization, the

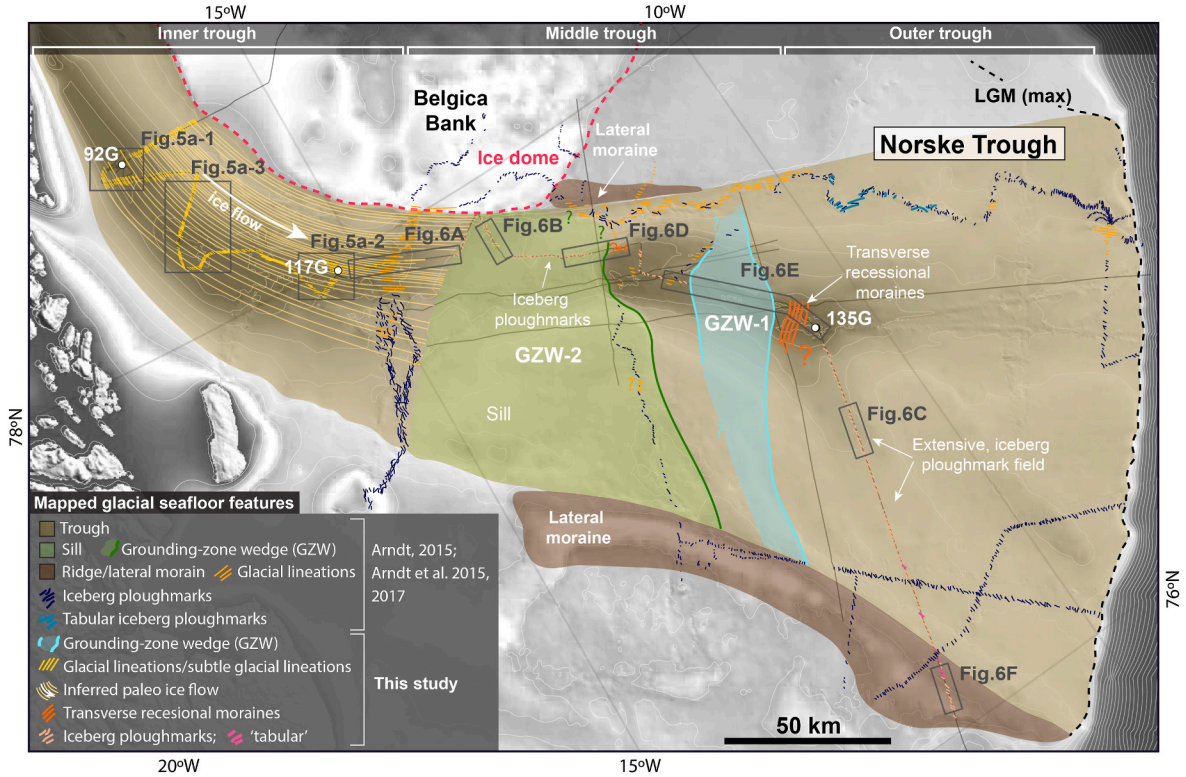


**Fig. 4.** Morphological map showing the distribution of glacial seafloor features in Norske Trough, NE Greenland shelf in relation to our sediment cores. Proposed last glacial maximum ice extents (LGM max; Evans et al., 2009; Arndt et al., 2017) is displayed. Bathymetric map extracted from Arndt et al. (2015). Ice dome outline is from Arndt et al. (2017).

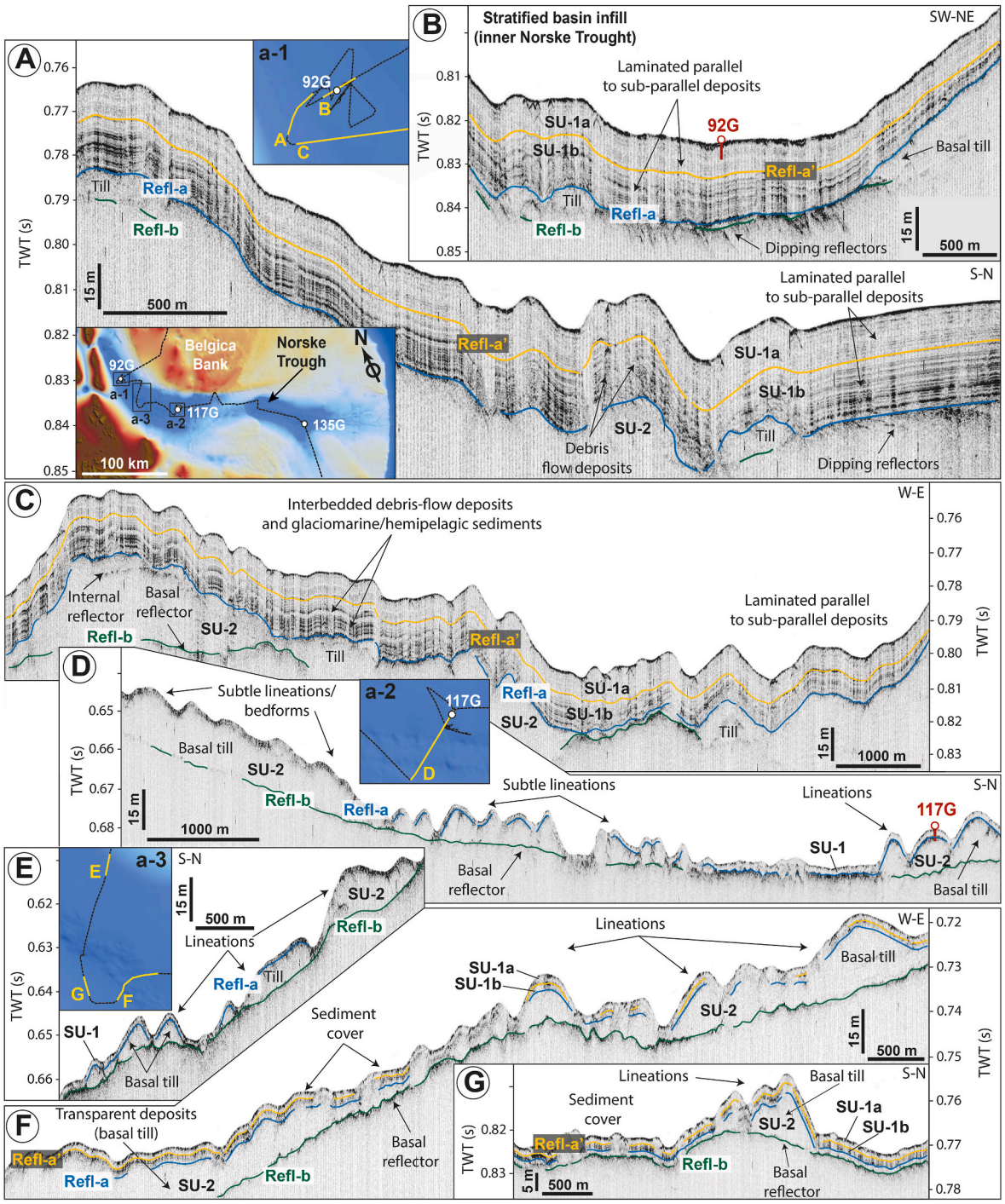


**Fig. 5.** High resolution seismic stratigraphic characterization and observed glacial features of the inner trough region. A), B) and C) Examples of a stratified (proglacial/glaciomarine sedimentation) basin infill (SU-1) located at the innermost trough. Note that burial subglacial landforms (glacial lineations) (SU-2) are often observed underlying the deglacial sediment pile. D), E), F) and G) Examples of glacial lineations aligned with the centerline of the trough (detailed ice flow in Fig. 4), note the length of lineations and the acoustically transparent facies (SU-2) interpreted as basal till suggest fast streaming ice. The location of SBP sections (in yellow) is indicated in added bathymetric sections (a-1, a-2 and a-3), while the location of the sediment cores is marked in dark red.

transverse and/or semitransverse ridges are interpreted as recessional moraines, formed at the grounding line during overall retreat with repeated short-term stillstands (Ó Cofaigh et al., 2008; Batchelor and Dowdeswell, 2015). Recessional moraines are typically associated with tidewater ice-sheet margins, as they require almost unlimited vertical accommodation space to build up at the grounding zone (e.g., Batchelor and Dowdeswell, 2015). In our data, the observed recessional moraines have a low-relief shape, suggesting that vertical accommodation space immediately beyond the grounding line was limited (e.g., Dowdeswell and Fugelli, 2012). According to Batchelor and Dowdeswell (2015), low-relief ridges are typically formed through restricting vertical accommodation space at low-angle roofed, water-filled cavities that exist between the seafloor and the base of ice shelves. Thus, the establishment of a floating ice shelf limiting the vertical accommodation space beyond the grounding line, as interpreted for the formation of GZWs, may have prevented the aggradation of high-relief recessional moraines. Moreover, the acoustically transparent character of these moraine ridges suggest a diamictic-like composition (Stewart and Stoker, 1990).

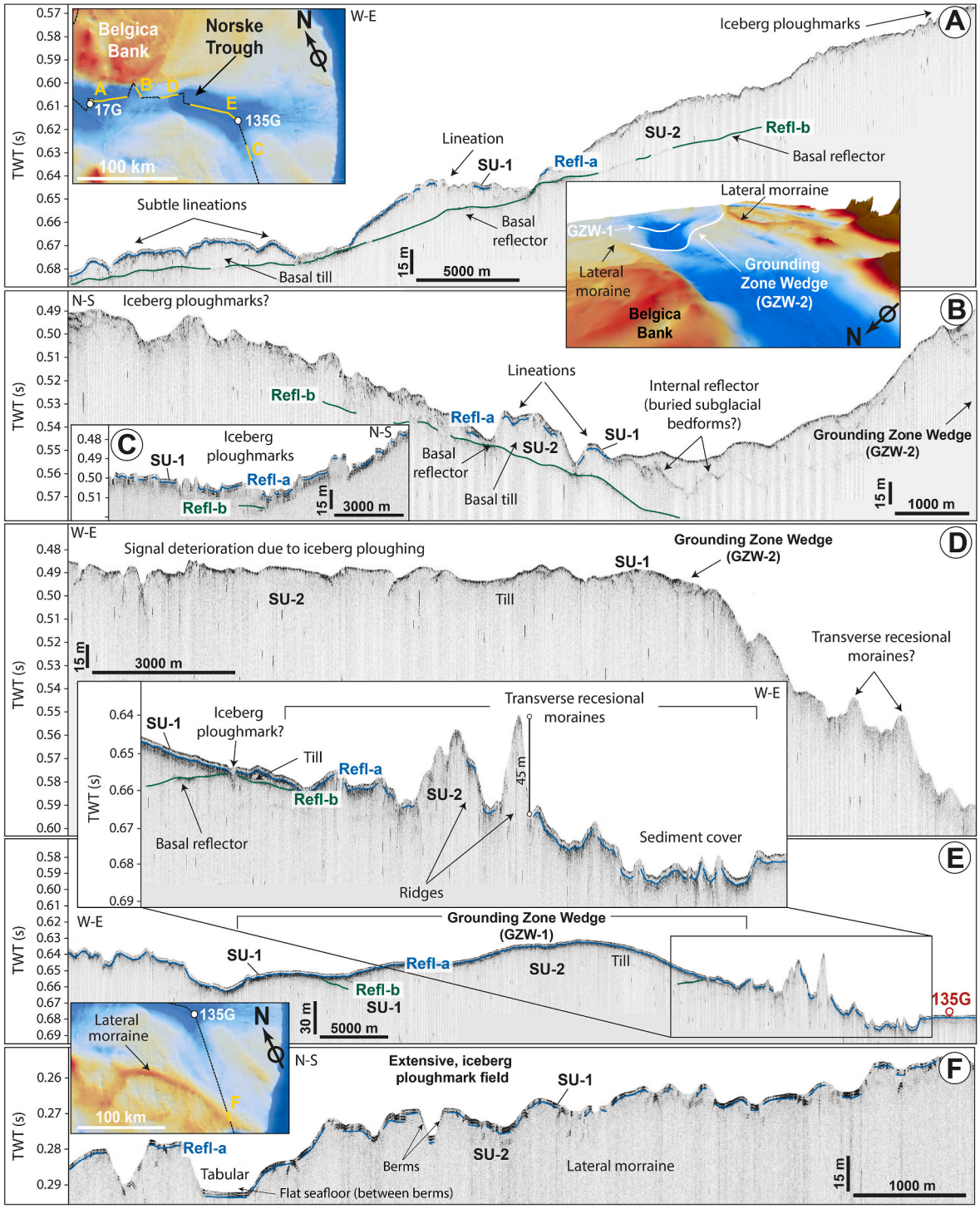


**Fig. 6.** High resolution seismic stratigraphic characterization and observed glacial features of the middle to outer trough region. A) and B) Glacial lineations. C) Iceberg ploughmarks. D) and E) Examples of the two observed grounding zone wedges (GZW-2 and 1), marking temporary ice stream stability during overall retreat. Paleo-ice flow was from left to right. Poorly defined seafloor due to iceberg ploughing is shown across the GZW-2. The enlarged area in (E) display a set of transverse recessional moraines oriented perpendicular to ice flow. F) Extensive, iceberg ploughmark field across the southern lateral moraine. Location of SBP sections (in yellow) is indicated in added bathymetric sections.

#### 4.3.4. *Iceberg ploughmarks*

Incisions, 'scours', are present in shallow areas of Norske Trough (e.g., overprinting GZW-2; Figs. 4 and 6D) and in the vicinity of the prominent, southern lateral moraine where they occur in high density (Figs. 4 and 6F). These scours mainly display characteristic U-shaped profiles, but also rectangular (tabular) shapes with flat central domains, often accompanied by adjacent berms (Fig. 6F). They are <500 m wide and ~5–20 m deep (Fig. 6F). Tabular shaped scours were documented only in the southern section of the outer trough (Fig. 4). Similarly, tabular shaped scours, interpreted as iceberg ploughmarks, were reported in the northern section of the outer trough by Arndt et al. (2017). The direction of the iceberg drift, as reported in detail by Arndt et al. (2017), is ~N–S, with likely both NE-SW and NW-SE directions (Fig. 4).

Based on the seismo-acoustic morphological characterization, the

mapped scours cross-cutting large-scale submarine landforms (e.g., GZW-2: Fig. 6D), are interpreted as iceberg ploughmarks formed later during the overall retreat by keels of drifting icebergs that have grounded into the uppermost sedimentary substrate of the seafloor (SU-1) along its path (Dowdeswell et al., 1993; Jakobsson et al., 2014). Moreover, documented tabular shaped ploughmarks in the outer trough (Arndt et al., 2017, Figs. 4 and 6F), suggest the release of calving, 'tabular' icebergs from regional floating ice shelves (e.g., Dowdeswell and Bamber, 2007). More recent scouring by icebergs originating from the Arctic Ocean may also occur.

### 4.4. AMS $^{14}C$ dating of cores 92G, 117G and 135G

The chronology of core 92G has been presented in Davies et al. (2022) (Table 1; S. Fig. 2A). The chronology for cores 135G and 117G is based on AMS $^{14}C$ measurements on both mixed species of benthic and mixed species of planktic foraminifera (Table 1; S. Fig. 2B and C). *Cassidulina neoteretis*, *Cassidulina reniforme* and *Elphidium clavatum* were the primary benthic foraminiferal species used for the AMS $^{14}C$ dating, while *Neogloboquadrina pachyderma* and *Globigerina bulloides* were the two planktic foraminiferal species used. In order to evaluate the potential loss of core top sediment during coring operations, we conducted a detailed stratigraphic/geochemical core-to-core correlation (i.e., between gravity and rumohr cores; S. Fig. 1), which indicated that ~9, ~9 and ~1 cm sediment was missing from the top of cores 92G, 117G and 135G, respectively.

The age-depth model of core 92G covers the last 13.4 cal Kyr BP (Davies et al., 2022), with the upper $^{14}C$-dated sample retrieved at 0.5 cm depth (597 cal Yr BP; S. Fig. 2A).

The age-depth model of core 117G indicates that the upper sedimentary succession covers the last 11.6 cal Kyr BP (i.e., the Holocene; S. Fig. 2B). However, the upper $^{14}C$-dated sample was obtained at 68 cm depth (7.07 cal Kyr BP; S. Fig. 2B). Absence of datable core material in the upper part of the succession (68–0 cm depth, lithological units II and I; S. Fig. 2B) does not allow precise middle-late Holocene interpretations. In addition, one radiocarbon-dated sample at 140 cm depth (i.e., the top of lithological unit VI), beyond the tie-point at 125 cm depth (11.57 cal Kyr BP), corresponds in age to the glacial period (22.1 cal Kyr BP; Table 1). Based on depositional processes interpreted for lithological unit VI (see below, Section 4.5.), we consider this $^{14}C$-date as redeposited and/or reworked from older sediments transported along debris flow deposits. In addition, and despite limited sample availability, two complementary $^{14}C$-dates at 272 and 329 cm core depth provided ages of 11.2 cal Kyr BP and 8.9 cal Kyr BP, respectively (Table 1). The first young $^{14}C$-date was obtained from lithological unit VI, which includes redeposited sediments transported along debris flow deposits. The second $^{14}C$-date, obtained from lithological unit VII, which is also interpreted as redeposited diamictic sediments (see below, Section 4.5.), provides an even younger $^{14}C$-date than the overlying dates, indicating a clear reversed pattern. Although it cannot be fully ruled out that reversal in the ages is linked to various degrees of mixing of old reworked and young in situ material, owing to the ultra-small sample size (<10 μg available carbon), we consider these three anomalous $^{14}C$-dates as unreliable and do not include them in our age model.

The age-depth model of core 135G covers the last 16.6 cal Kyr BP (i.e., the very late Pleistocene and the Holocene; S. Fig. 2C). However, the upper radiocarbon-dated sample was obtained at 65 cm depth (2.17 cal Kyr BP; S. Fig. 2C). Absence of datable core material in the upper part of the sedimentary succession (65–0 cm depth, mainly lithological unit I; S. Fig. 2C), does not allow precise late Holocene interpretations. In contrast, the radiocarbon-dated sample at 210 cm depth (16.65 cal Kyr BP; S. Fig. 2C), right above lithological unit VII, allows us to interpret major pre-Holocene events (i.e., the Bølling-Allerød warm period and the Younger Dryas cold period). In addition, two radiocarbon-dated samples in the bottom part of the sedimentary succession (i.e., within lithological unit VII at depths of 222 and 274 cm) indicate Pleistocene deposition (~28.2 to >41 cal Kyr BP; S. Fig. 2C). Based on depositional processes interpreted for lithological unit VII (see below, Section 4.5.), we consider these pre-LGM $^{14}C$-dates as redeposited and/or reworked from older sediments transported along the base of an ice stream.

### 4.5. Lithostratigraphy of the uppermost trough strata

Seven lithological/sedimentological (lithofacies) units (LU) have been defined from the core bottom upward based on lithological composition, sedimentary structures and geochemical/physical properties changes: LU-VII, LU-VI, LU-V, LU-IV, LU-III, LU-II and LU-I (Figs. 7 and 8 and S. Figs. 3–5).

#### 4.5.1. LU-VII – massive, matrix-supported soft diamicton

LU-VII is the lowermost lithological unit observed in two of the three investigated cores (135G and 117G). It comprises a distinctive reddish to dark reddish brown, massive, matrix-supported diamicton with bimodal distribution and a sandy mud matrix of <5 cm angular to sub-angular, randomly oriented clasts (Figs. 7, 8 A-E). Crystalline rocks and grains with hematite coatings (mainly quartz and feldspars), with minor amounts of metamorphic and volcanic rocks (e.g., quartzites/basalt), mica, olivine grains, and volcanic glass shards, characterize the diamictic composition of LU-VII (Fig. 8B and C). Foraminifera occur very rarely. The upper unit boundary is sharp and there are no signs of bioturbation (Fig. 7). The sediment grain size is dominated by the sand and silt fractions, rather than clay, throughout this unit (S. Figs. 3 and 4). Magnetic susceptibility (MS), density and shear strengths values (core 135G: 100–162; core 117G: 140–170 kPa) are comparatively higher than in the overlying lithological unit (S. Figs. 3 and 4), suggesting sediment over-consolidation. Terrigenous elements (Ti, K, Si, Al, Fe) and Ca, Sr, Ba, and other elemental ratios (e.g., K/Ti, Ca/Sr or Ca/K), exhibit a bottom-up decreasing trend up to 255 cm depth, followed by a general increasing trend towards the top unit in core 135G (Fig. 7 and S. Figs. 3 and 4). In core 117G, the elements/elemental ratios show no significant variability until the top 10 cm where terrigenous elements (e.g., Ti) increase while Ca and Sr decrease (Fig. 7 and S. Fig. 4).

Petrographic grain composition, including XRF-measured elemental composition, suggests mid-Devonian sand and siltstones (red beds) of the NE Greenland hinterland as the source area of these diamictons (Fig. 1A; Bond and Lotti, 1995; Hubberten et al., 1995; Stein, 2008; Stein et al., 2016; Syring et al., 2020); previously interpreted as 'diamictic basal till' deposited at the base of an ice stream in both the E and NE Greenland shelf (e.g., Stein, 2008; Syring et al., 2020, respectively). Moreover, the recognition of (diamictic) particle-size distributions with a bimodal character, which is indicative of comminution processes involving particle size reduction by crushing and abrasion, is a common observation in subglacial tills (e.g., Dreimanis and Vagners, 1971; Haldorsen, 1981; Larsen et al., 2004; Piotrowski et al., 2006; Madsen and Piotrowski, 2012). Based on the diamictic composition, bimodal grain-size distribution, large amounts of angular to sub-angular clasts along with the homogeneity in the matrix material, high shear strength, absence of bioturbation and the sharp contact with overlying sediments (LU-VI), we interpret LU-VII as a diamictic subglacial basal till deposited at the base of an ice stream (Anderson et al., 1980; Anderson, 1999; Dowdeswell et al., 2004; Ó Cofaigh et al., 2005; Evans et al., 2006; Stein, 2008; Evans, 2018). In addition, core 117G was recovered from a field of glacial lineations, which is well known as a paleo-subglacial geomorphic setting (Figs. 4 and 5D). Accordingly, seismo-acoustic morphological results (Sections 4.2. and 4.3.) also support this interpretation. Furthermore, the well-defined (red-colored; Fig. 7) diamictic composition rule out transport by single icebergs, which would result in a more mixed type of sediment (Bond and Lotti, 1995; Stein, 2008).

#### 4.5.2. LU-VI – massive sandy mud with interbedded matrix-supported, diamictic-like horizons

This unit was only recovered in core 117G (Fig. 7). LU-VI is

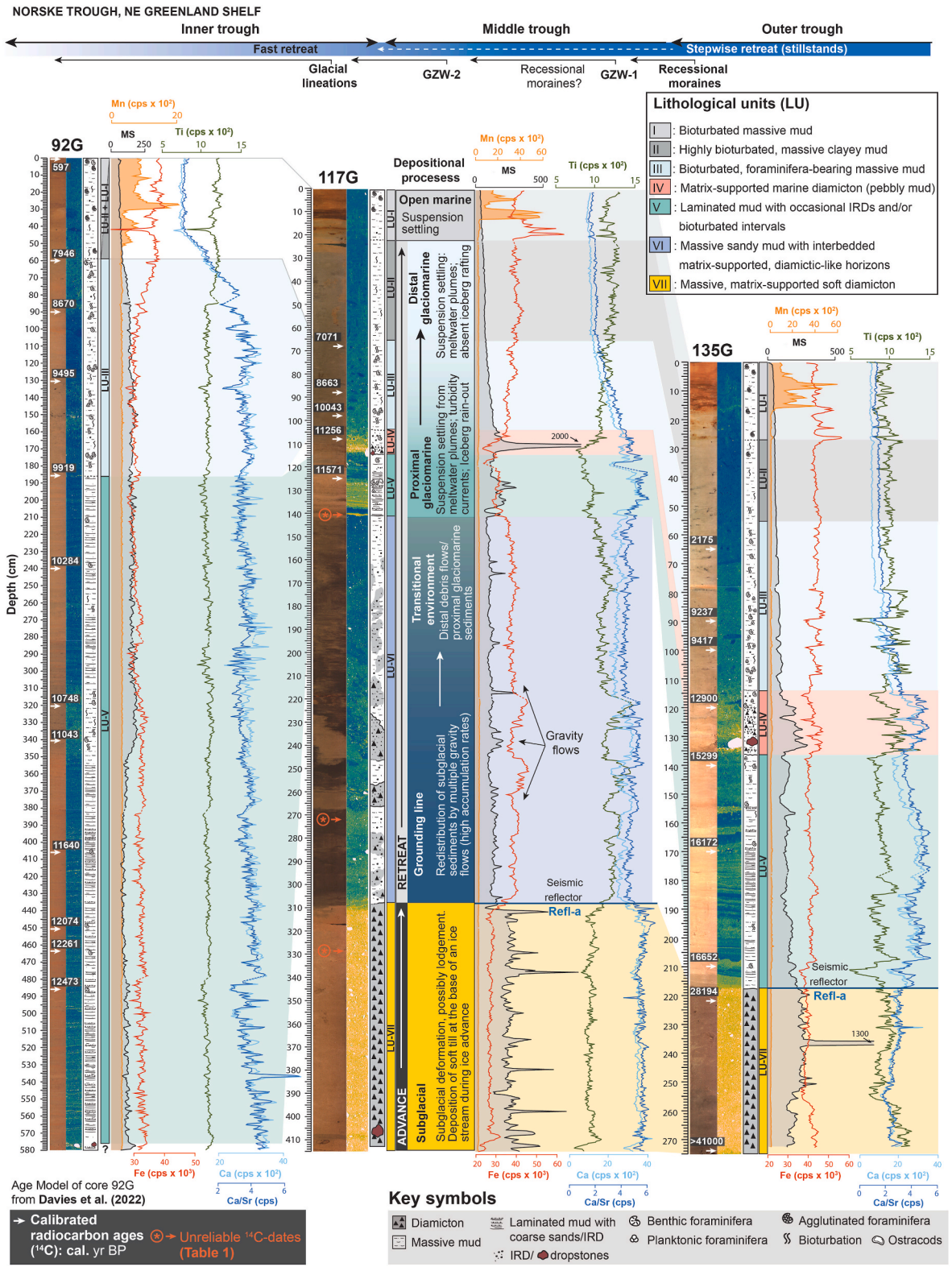


**Fig. 7.** Detailed stratigraphic log/correlation of gravity cores 92G, 117G and 135G. From left to right: high-resolution digital images with calibrated radiocarbon ages ($^{14}$C cal. Yr BP; white arrows), CT scans, graphic lithological logs, lithological units (LU), and bottom-up variations in magnetic susceptibility and selected XRF-scan data. For complete information see Supplementary Material (S. Figs. 3–5). Note that depositional processes are also included.

composed of dark gray massive sandy mud with interbedded reddish brown, massive, matrix-supported diamictic-like horizons. The lower- and upper-unit boundaries are sharp, while bioturbation and foraminifera occur very rarely (Fig. 7). Poorly sorted, sandy mud with <3 cm sub-angular, randomly oriented clasts, and similar petrographic composition than underlying LU-VII, characterize the diamictic-like horizons (Figs. 7 and 8F). Moreover, diamictic-like horizons are contorted by sharp to irregular (erosional) contacts (Fig. 8F). The sediment grain size is slightly dominated by the silt fraction, with noticeable peaks of sand comprising the diamictic-like horizons (S. Fig. 4). MS and

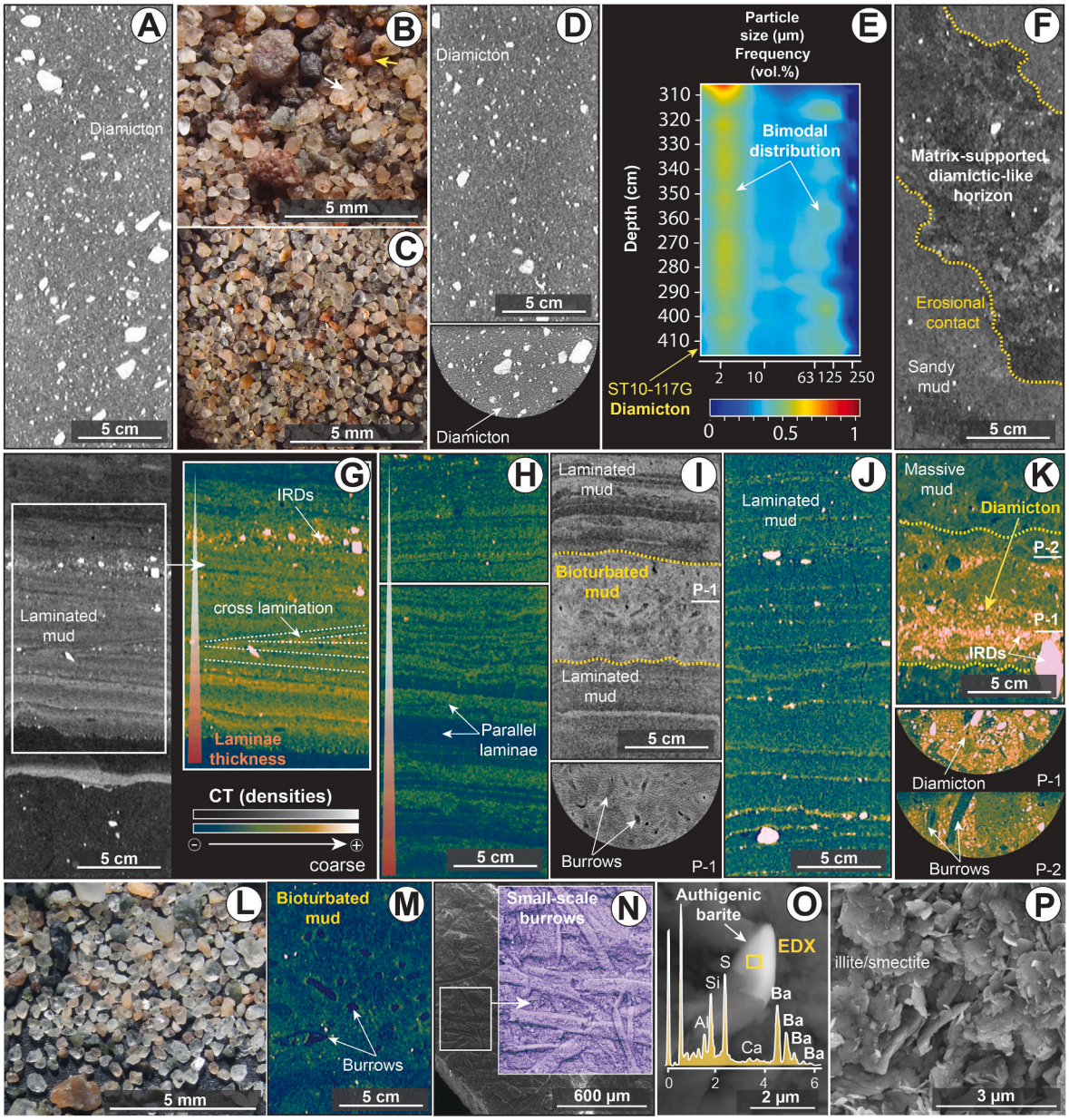


**Fig. 8.** Sedimentation at the studied Norske Trough sedimentary sections. A) CT scan example of LU-VII (core 117G, 328–355 cm depth) showing massive, matrix-supported soft diamicton (subglacial basal till). B) and C) Binocular microscope photomicrographs showing detailed, sieved (>250 μm) grains from the diamictic LU-VII (core 117G; 413 and 333 cm depth, respectively). Crystalline rocks/grains with hematite coatings (e.g., quartz: white arrow; feldspars: yellow arrow), with minor amounts of metamorphic/volcanic rocks and mica, olivine grains and volcanic glass shards, characterize the diamictic composition. D) CT scan example of LU-VII (core 135G, 230–248.5 cm depth) showing massive, matrix-supported soft diamicton. E) Example of bimodal grain-size distribution of LU-VII (diamicton; core 117G). F) CT scan example of LU-VI (core 117G, 225–250 cm depth) showing massive sandy mud with interbedded matrix-supported, diamictic-like horizons (debris-flow deposits). G), H), I) and J) CT scan imageries of LU-V displaying detailed laminated mud with occasional IRD and/or bioturbated intervals (G: core 117G, 121–147 cm depth; H and I: core 135G, 170–193 and 186–226 cm depth; J: core 92G, 533–558 cm depth). Note that faint cross lamination is also observed in core 117G (133 cm depth). K) CT scan example of LU-IV (core 117G, 103–116 cm depth) showing matrix-supported iceberg rafted diamicton. L) Binocular glass photomicrograph showing sieved (>250 μm) grains from the diamictic (iceberg rafted) LU-IV (core 117G, 108 cm depth). M) CT scan example of LU-III (core 92G, 133–146.3 cm depth) displaying bioturbated, foraminifera bearing massive mud. N) SEM photomicrograph (SE) showing burrowed clayey mud of LU-II (core 117G, 40 cm depth). O) SEM (BSE) photomicrograph and related energy dispersive X-ray (EDX) analysis of euhedral to sub-spherical (authigenic) barite observed in LU-II (core 117G, 40 cm depth). P) SEM photomicrograph (SE) of LU-I showing the clay-sized matrix dominated by illite/smectite (core 117G, 11 cm depth).

density values are comparatively much lower than in the underlying lithological unit, with slightly higher values comprising the diamictic-like horizons (Fig. 7). Terrigenous elements (Ti, K, Si, Al, Fe) and Ca, Sr, and other elemental ratios (e.g., Fe/K, K/Ti, Ca/Sr or Ca/K) show no significant variability thorough, except for the diamictic-like horizons (Fig. 7 and S. Fig. 4). Ba and Mo (incoherent/coherent scattering ratio; inc/coh), however, exhibit a bottom-up increasing and decreasing trends respectively (S. Fig. 4). In the diamictic-like horizons, terrigenous elements (e.g., Ti) and other elemental ratios (e.g., K/Ti) decrease, while Ca and Sr and other elemental ratios (e.g., Ca/Sr and Ca/K) increase.

Textural and mineralogical similarities of interbedded diamictic-like horizons within LU-VI and underlying diamictic subglacial basal till (LU-VII) leads us to the interpretation that these are debris flow deposits originating from melt-out of englacial debris at the adjacent grounding

line (Domack et al., 1999; Evans and Pudsey, 2002; Pudsey et al., 2006; Smith et al., 2017, 2019; Prothro et al., 2018); which is comparable to the sub-ice shelf sedimentary sequence ascribed as 'stratified diamicton' by Smith et al. (2019). Comparable sedimentary archives comprising a basal overconsolidated subglacial till, overlain by mud with interbedded diamictic-like horizons and interpreted as debris-flow deposits, have been reported in the study area and regionally (e.g., Stein, 2008; Syring et al., 2020). Alternatively, and taking into account that core 117G is located 29 km behind GZW-2 (Fig. 4), stacking of successive debris flows at LU-VI could be the result of gravity-driven downslope processes from the earlier stages of adjacent GZW-2 topset. Another possible explanation is that LU-VI reflects an ice-proximal setting with a glaciomarine sedimentation containing large amounts of IRD associated to episodic calving events. However, diamicton textural and mineralogic homogeneity (including XRF-measured elemental concentration) in LU-VII and LU-VI rule out transport by single icebergs which would result in a more mixed type of sediment (Bond and Lotti, 1995; Hubberten et al., 1995).

#### 4.5.3. LU-V – laminated mud with occasional IRD and/or bioturbated intervals

LU-V is found in all three cores, and it makes up the bottom unit of core 92G. The unit consists of yellowish-to reddish-brown laminated to stratified mud with occasional granule/pebble clasts and interbedded bioturbated intervals (Figs. 7, 8G-J). Lamination, 4–10 mm thick, is composed of parallel laminae with alternating coarse and fine mud, which exhibit, respectively, lighter and darker X-ray attenuations (densities) on the CT scan images (Fig. 8G–J). Faint cross lamination is also observed in core 117G at 133 cm depth (Fig. 8G). Above 181 cm depth (core 135G) and 135 cm depth (core 117G), respectively, laminae thickness displays a slightly bottom-up decreasing trend, and the finer laminae become thicker than their coarse counterparts (Fig. 8G and H). However, in core 117G a thicker coarse lamina with large amounts of sandy grains is noticed at 127 cm depth (Fig. 8G). Similarly, laminations with fine grains become dominant above 390 cm depth in core 92G (Fig. 7; Davies et al., 2022). Normally graded laminae are observed throughout (Fig. 8G–J). The lower unit boundary is sharp, while the upper unit boundary is gradational and display diffuse laminae (Figs. 7 and 8G). Sediments are composed of mostly terrigenous components, including angular to sub-angular grains of quartz and feldspar with subordinate, undifferentiated metamorphic and volcanic rock fragments, olivine and mica. Foraminiferal occurrence is rare to moderate. In cores 135G and 117G, the silt fraction dominates the sediment grain size, while the clay fraction slightly predominates over the silt-sand fractions in core 92G (S. Figs. 3–5). MS and density values in cores 135G and 117G are comparatively higher than in the underlying unit, with noticeable peaks (Fig. 7 and S. Figs. 3 and 4). In core 92G, MS and density values show no significant variability but increase from 350 cm depth, coincident with a bioturbated interval (Fig. 7; S. Fig. 5). Terrigenous elements (Ti, K, Si, Al) and Ca, Sr, and other elemental ratios (e.g., K/Ti, Ca/Sr or Ca/K) fluctuate considerably, while even greater variability is found in core 135G (Fig. 7 and S. Figs. 3–5). In this core, elements/elemental ratios (Ti, Al, K, Si, Ca, Sr, K/Ti, Ca/Sr, Ca/K) display an overall bottom-up increasing trend with minor fluctuations and noticeable peaks from 195 to 170 cm depth, coinciding with the more condensed laminated interval (Fig. 8H), followed by a general decreasing trend toward the top unit (S. Fig. 3). Similarly, in core 117G a slightly bottom-up increasing trend is followed by a decreasing trend of elements/elemental ratios (Ti, Al, K, Si, Ca, Sr, Ca/Sr, Ca/K) (S. Fig. 4).

Several proxies indicate that LU-V is largely terrigenous in origin. High elemental counts of terrigenous elements (Ti, K, Si, Al, Fe) and K/Ti ratios have been related to higher supplies of detrital sediments (e.g., Rothwell and Croudace, 2015; Bertram et al., 2018; López-Quirós et al., 2021). Also, high K/Ti ratios indicate an increased influx of illite-rich particles (e.g., Diekmann et al., 2008; López-Quirós et al., 2021) mostly supplied by physical weathering. Illite-rich clay fractions along with higher MS and density values suggest a close relationship between grain size and physical properties, which also supports a dominantly terrigenous depositional regime. LU-V is interpreted to contain proximal glaciomarine sediments deposited from terrigenous suspension settling. This is based on its fine-grained nature and largely rhythmic parallel lamination imparted by alternating coarse and fine laminae of mud (Domack et al., 1999; Ó Cofaigh and Dowdeswell, 2001; Ó Cofaigh et al., 2001; Prothro et al., 2018; Smith et al., 2019). Laminated mud intervals, related to suspension settling from meltwater plumes, are frequently deposited in a grounding line proximal setting (e.g., Forwick and Vorren, 2009; Streuff et al., 2018; Davies et al., 2022). The stratification of sediments suggests variations in the current strength of the water masses emanating from the ice margin. The bottom-up decrease in laminae thickness as well as the decrease in thickness of coarse laminae, suggest a reduced sedimentation rate triggered by minor grounding line retreat and a gradually ice-distal sediment source (e.g., Ó Cofaigh et al., 2001; Streuff et al., 2017, 2018), from which larger amounts of fine-grained sediments possibly reached the studied core sites. Moreover, reported foraminiferal species in core 92G (Davies et al., 2022), which are often found beneath floating ice sheets or perennial sea ice (e.g., Jennings et al., 2020; Polyak et al., 2002), further suggest deposition by suspension settling from meltwater plumes under a floating ice shelf. Although, the thinner laminated sequence, when compared to other Arctic sub-ice shelf records (e.g., in Nares Strait, where ice shelf laminated lithofacies are up to 15 m thick; Jennings et al., 2022) suggests a limited or less extensive depositional process by suspension settling from meltwater plumes. The occurrence of diffuse faint cross lamination in core 117G (Fig. 8G), which suggest sediment deposition from turbidity currents alongside suspension settling, cannot be ruled out (Gilbert et al., 1993; Ó Cofaigh and Dowdeswell, 2001; Talling et al., 2012). In addition, occasional occurrence of granule and pebble clasts within laminated muds likely indicate debris sourced from subglacial meltwater beneath the ice shelf (Jennings et al., 2022).

#### 4.5.4. LU-IV – matrix-supported marine diamicton (pebbly mud)

This unit was recovered only in two of the three inspected cores (135G and 117G). LU-IV consists of brown to greenish-brown, matrix-supported diamicton or 'pebbly mud' (Figs. 7 and 8K, L). Sediments are mostly composed of terrigenous components, including sub-angular grains of quartz/feldspar and undifferentiated metamorphic and volcanic rock fragments (Fig. 8L). The lower unit boundary is sharp-to-irregular, whilst from 115 cm depth (core 135G) and 105 cm depth (core 117G) upwards, the diamicton gradually fines upward into bioturbated, foraminifera bearing massive mud (overlying LU-III; Fig. 7). Accordingly, moderate burrowing activity is observed at the upper part of LU- IV (e.g., Fig. 8K). Benthic foraminifera (calcareous) are abundant and diverse in the upper part of the unit toward the transition to the overlying LU-III (Fig. 7). The sediment grain size is dominated by the silt fraction, with conspicuous peaks of sand (S. Figs. 3 and 4). MS and density values are relatively higher than in the underlying unit (Fig. 7 and S. Figs. 3 and 4). Terrigenous elements (Ti, K, Si, Al, Fe) and Ca, Sr, and other elemental ratio (e.g., K/Ti, Ca/Sr, Ca/K) in core 135G exhibit a general bottom-up increasing trend up to 121 cm depth, followed by a decreasing trend towards the top of the unit, where increasing bioturbation is also observed (Fig. 7 and S. Fig. 3). Similarly, a bottom-up increasing trend in terrigenous elements, followed by a slightly decreasing trend in elements/elemental ratios (e.g., Si, K, Ca, Sr, Ca/Sr, Ca/K), characterizes core 117G (S. Fig. 3).

Several proxies indicate that LU-IV is, as interpreted in the underlying unit, mainly terrigenous in origin. LU-IV is interpreted to have been deposited in an ice-proximal glaciomarine environment by vigorous iceberg rafting as the calving zone of a floating ice shelf passed over core sites 135G and 117G (Domack et al., 1999; Kilfeather et al., 2011; Yokohama et al., 2016; Smith et al., 2011, 2019). However, an alternative interpretation would be that the deposition of pebbly muds (LU-IV), overlying laminated muds (LU-V) may correspond to a period of enhanced melting of debris-rich basal ice at the grounding zone as turbid

meltwater plumes (e.g., Reilly et al., 2019), as suggested in other Arctic ice shelf lithofacies records (e.g., at Petermann Fjord/northern Nares Strait; Jennings et al., 2022). In this case, the retreating calving-line hypothesis is favored relative to a period of basal melting due to differences in petrographic composition between LU-IV and the underlying lithological units, such as the diamictic-like horizons of LU-VI, interpreted to be deposited by melt-out of englacial debris (see above). For example, the mineralogical composition of LU-IV is devoid of quartz and feldspars with hematite coatings, which are the dominant grains found in LU-VI and in the diamictic subglacial basal till (LU-VII). In contrast, Ca/Sr spikes observed in LU-IV suggest an increased delivery of IRD rich in detrital carbonate. Accordingly, we interpret LU-IV as an iceberg rafted diamicton. This iceberg rafted diamicton (LU-IV), overlying laminated muds deposited by suspension settling from meltwater plumes (LU-V), is part of the idealized Antarctic sub-ice shelf lithofacies model (Fig. 3 in Smith et al., 2019). Differences between Antarctic and Arctic ice shelf lithofacies models are most likely due to the scale of the ice shelves in each region, which may also limit depositional processes such as sedimentation by turbid meltwater plumes (see Jennings et al., 2022, for a thorough review of similarities and differences between models). Given the size of Norske Trough, covering about 20% of the NE Greenland shelf, compared to Greenland's modern ice tongues that are confined within fjords (e.g., Jennings et al., 2022), and the thinner and less extensive nature of underlying laminated muds (LU-V) that suggest limited meltwater processes in cores 135G and 117G, we consider the Antarctic sub-ice shelf model of Smith et al. (2019) to be the more conservative interpretation. Moreover, the deposition of biogenic muds (LU-III) overlying LU-IV, interpreted to have been deposited in an ice-distal glaciomarine to open marine environment (see below), supports retreat of the ice shelf calving front back from sites 135G and 117G.

#### 4.5.5. LU-III – bioturbated, foraminifera-bearing massive mud

LU-III is composed of massive brown mud with moderate bioturbation (Figs. 7 and 8 M). High occurrence of IRD is observed in core 92G from 185 to 130 cm depth (S. Fig. 5), while only rare occurrences are noticed in cores 117G and 135G (S. Figs. 3 and 4). Both the lower and upper contact boundaries are gradational (Fig. 7). Well-preserved benthic and planktonic foraminifera are abundant (Fig. 7). In addition, the lower part of LU-III in core 92G is dominated by the shallow-infaunal benthic species *Cassidulina neoteretis* (Seidenkrantz, 1995), as shown in Fig. 6 of Davies et al. (2022). In cores 135G and 117G, the silt fraction dominates the sediment grain size, while in core 92G the clay fraction slightly predominates over the silt fraction (S. Figs. 3–5). MS and density values are lower than in the underlying unit and exhibit a slightly bottom-up decreasing trend in cores 135G and 117G (Fig. 7 and S. Figs. 3 and 4). In core 92G, MS and density values exhibit similar decreasing bottom-up trends but with major fluctuations (e.g., density values decrease up to 95 cm depth followed by an increasing trend toward the top of the unit) (Fig. 7 and S. Fig. 5). Terrigenous elements and Mo (inc/coh) and Ba, and other elemental ratios (e.g., Fe/K or Fe/Ca) display an overall bottom-up increasing trend with minor fluctuations, while greater variability characterizes core 135G (Fig. 7 and S. Figs. 3 and 4). Ca, Sr, and other elemental ratios (e.g., Ca/Sr and Ca/K) exhibit a bottom-up decreasing trend (Fig. 7 and S. Figs. 3 and 4). Major fluctuations characterize core 92G, although from 115 cm depth toward the top unit Ca and Ca/Sr and C/K ratios decrease while Fe/Ca ratio increase (Fig. 7 and S. Fig. 5).

LU-III is interpreted to reflect terrigenous suspension settling in an ice-distal glaciomarine to open marine environment, with limited contribution from iceberg or sea-ice rafting at middle to outer shelf positions (e.g., Kilfeather et al., 2011; Hogan et al., 2016). Moreover, reported dominance of *Cassidulina neoteretis* in core 92G (Davies et al., 2022), which in Arctic settings is a well-known indicator of Atlantic Water influx (e.g., Seidenkrantz, 1995; Hald and Korsun, 1997; Syring et al., 2020; Davies et al., 2022; Rasmussen et al., 2022; Hansen et al., 2022; Cage et al., 2021), suggest an increased influence of Atlantic Water at the seafloor after 11.2 cal Kyr BP (Fig. 7), either due to increased influx of Atlantic water or decreased impact of the glacier melt water. Based on our core-to-core comparison (Fig. 7), a similar increase in Atlantic Water influence may have occurred from the outer to middle shelf after 12.9 cal Kyr BP.

#### 4.5.6. LU-II – highly bioturbated, massive clayey mud

LU-II consists of massive mud with moderate bioturbation and very rare-to-absent occurrence of IRD (Fig. 7). The unit displays an olive gray color in cores 135G and 117G, while in core 92G it is reddish-brown in color (Fig. 7). Diverse vertical burrows and escape traces are observed throughout all three cores (Figs. 7 and 8 N). Calcareous foraminifera are absent in this unit (Fig. 7). The lower unit boundary is gradational in all three cores while the upper unit boundary is sharp in cores 135G and 117G and gradational in core 92G (Fig. 7). Sediment grain size is largely dominated by the silt fraction, which exhibit a bottom-up increasing trend in cores 135G and 117G, while in core 92G the silt and clay fractions display similar proportions (S. Figs. 3–5). Moreover, abundant euhedral to sub-spherical barite grains were observed in core 117G (Fig. 8O). MS and density values are similar to the underlying top lithological unit and also display a slightly bottom-up decreasing trend (Fig. 7 and S. Figs. 3–5). Terrigenous elements (Ti, K, Si, Al, Fe) and Ca, Sr, and other elemental ratios such as K/Ti, Ca/Sr or Ca/K in cores 135G and 117G display no significant variability, while Ba and Mo (inc/coh) exhibit a weak bottom-up increasing trend (Fig. 7 and S. Figs. 3 and 4). No major fluctuations are observed in core 92G, although from the bottom of the unit up to 45 cm depth terrigenous elements (e.g., Ti, Al, Si, Fe and K) and Ca and Ca/Sr and C/K ratios decrease while Fe/K and Fe/Ca ratios increase (Fig. 7 and S. Fig. 5).

LU-II is interpreted to have been deposited, as in LU-III, in an ice-distal glaciomarine to open marine environment. However, with increased distance from the grounding line, deposition from turbid meltwater plumes typically grade into more bioturbated, massive clayey muds (e.g., Ó Cofaigh and Dowdeswell, 2001; Prothro et al., 2018; Smith et al., 2019). Accordingly, we interpret a more distal paleoenvironmental setting dominated by hemipelagic/pelagic sedimentation during deposition of LU-II. In addition, data from core 92G (Davies et al., 2022) provide evidence for a period of increased perennial sea ice cover and reduced marine productivity on the innermost shelf. In contrast, several proxies in cores 135G and 117G indicate that LU-II was deposited from inner to outer shelf positions under enhanced productivity water conditions. Relatively higher elemental counts of Ba indicate that primary productivity was enhanced in surface waters (e.g., Röhl et al., 2007; Ziegler et al., 2010). Additionally, occurrence of authigenic barite grains in core 117G (Fig. 8O) likely indicate high levels of primary productivity in surface waters, as the occurrence of marine (authigenic) barite in oxic-pelagic sediments has been related to high-bio productivity regions (e.g., Dymond et al., 1992; Paytan and Griffith, 2007; López-Quirós et al., 2021). Also, the olive (greenish) coloration of LU-II in cores 135G and 117G is diagnostic of deposition during a period of higher biological productivity (Kilfeather et al., 2011; Smith et al., 2011). This increased productivity could have been triggered by a rise in ocean temperatures (Hogan et al., 2016). Likewise, the very rare occurrence of IRD may likely be the effect of incursions of warm subsurface waters, triggering open-water conditions (Syring et al., 2020).

#### 4.5.7. LU-I – bioturbated, massive mud

LU-I is composed of dark brown to yellowish-brown massive mud, with moderate bioturbation and very rare to absent occurrence of IRD (Fig. 7). Calcareous foraminifera are absent throughout, although agglutinated foraminifera are observed at the very top of the unit near the seafloor (Fig. 7). Sediment grain size is largely dominated by the silt fraction, which shows a bottom-up increasing trend in cores 135G and 117G, while in core 92G the silt and clay fractions show equal proportions (S. Figs. 3–5). MS and density values are similar to the

underlying unit with no significant fluctuations (Fig. 7 and S. Figs. 3–5). Terrigenous elements (e.g., Ti, K, Si, Al), Ca, Sr, and elemental ratios (e.g., K/Ti, Ca/Sr, Ca/K) display no significant fluctuations, although a prominent interbedded dark brown Mn-rich band is depicted in both digital images and XRF data (Fig. 7 and S. Figs. 3–5). Moreover, a number of ochre colored Fe-rich layers are observed underlying the Mn-rich interval (Fig. 7). Also, noticeable peaks in Fe/K and Fe/Ca ratios are recorded at the Fe-rich layers in cores 135G and 117G (S. Figs. 3 and 4).

LU-I was likely deposited in an open marine environment by hemipelagic suspension settling. A major paleoredox change at the top ~20 cm of LU-I is interpreted from resulting buried Fe/Mn oxide discontinuities as indicated by the elemental counts of Fe and Mn (e.g., Richter et al., 2006; Wolters et al., 2010). The observation of comparable buried Fe/Mn oxide discontinuities in the uppermost 50 cm of sediments from the Atlantic, Pacific or Central Arctic oceans (e.g., Burdige, 1993; März et al., 2011; Löwemark et al., 2014), have been attributed to warmer (interglacial) climate conditions and related physical/biogeochemical processes in the water column and seafloor. Macdonald and Gobeil (2012) in their source-to-sink study with reference to periodic remobilization and re-precipitation of Mn in basin sediments from the Arctic Ocean, stated that almost all the non-lithogenic Mn, subject to redox transformations, enters from land via riverine input or coastal erosion. However, only a minor fraction of this Mn is trapped in surface shelf sediments to form Mn-rich bands. Accumulation of Mn in these enriched-bands results from reduction of $Mn^{(IV)}$ to soluble, mobile $Mn^{(II)}$, facilitated by relatively high fluxes of labile $C_{Org}$ to sediments consuming dissolved $O_2$ through metabolism. Trapped Mn in surface shelf to slope sediments is ultimately transported to and buried deeply in the interior basin sediments where $C_{Org}$ fluxes are extremely low to account for reduction of available $Mn^{(IV)}$. They proposed Holocene sea-level rise as a likely forcing mechanism of Mn-rich banding formation in Central Arctic Ocean (Macdonald and Gobeil, 2012). Further detailed investigations are required to interpret triggering factors of the Fe/Mn oxide discontinuities found at our study site, but a comparable environment of low-productivity and oxygenated bottom waters, with deep $O_2$ penetration depths, and trapping of almost all settling Fe/Mn oxides to our core site location is plausible.

## 5. Discussion

### 5.1. Maximum ice stream extent: new insights

Glacial lineations, extending almost to GZW-1 in the middle to outer trough (this study), together with a set of recessional moraines on an outer shelf position (Fig. 4), indicate that a grounded, fast-flowing ice stream extended at least to an outer shelf position. Likewise, interpreted subglacial basal till/debris in cores from the inner to outer trough (cores 117G and 135G; Figs. 7, 8 A-E), demonstrate that subglacial and subaqueous processes adjacent to an ice stream grounding line were active at those shelf positions. In addition, glacial landforms on either side of the middle to outer trough appears continuous, suggesting that the GZWs represent stillstands during one glacial cycle (i.e., during the LGM; see below), rather than the separation of two distinct assemblages from different glacial cycles. A date on the top of the interpreted subglacial basal till in core 135G, located in front of the outer GZW-1 (Fig. 4), provides a maximum age for this advance, and indicates that it occurred before 16.6 cal Kyr BP (Fig. 7), and thus likely during the global LGM (26.5–19 cal Kyr BP; Clark et al., 2009). This contrasts with an accepted conceptual model, missing morphological evidence, that suggests an ice stream extent restricted to an inner trough position in the study area during the LGM (Funder et al., 2011, Fig. 1B).

Sediment cores from the NE Greenland continental slope suggest that the maximum glaciation, with highest amount of IRD and high input of terrigenous material, occurred between 21 and 16 cal Kyr BP (Stein et al., 1996; Spielhagen and Mackensen, 2021). In Norske Trough, our combined seismic and sedimentological data suggest that during the LGM, the GrIS reached its maximum extent somewhere on the outer shelf and may even have reached the shelf edge (Figs. 4 and 9A). Hence, we suggest that Norske Trough was filled by grounded ice masses, derived from the areas presently occupied by the floating ice tongue of the 79°-Glacier (i.e., its adjacent bay) and the Jøkelbugten Fjord into which the Zachariae Isstrøm drains today (Fig. 1B). Besides, the remaining physiography at Germania Land (southwest of Norske Trough) suggests that major areas of its ice cover were drained via Skærfjorden as a tributary to the southern Norske Trough (Landvik, 1994; Arndt et al., 2017) (Fig. 1B). The limited SBP sections that we recovered from the outer Norske Trough (Fig. 1B), and the fact that the sediments shown in these profiles have been almost entirely reworked by the ploughing action of iceberg keels (e.g., Fig. 6D, F), means that we at present can only provide little new information about the ice extent and character on the continental shelf beyond the inner part of the outer trough (Fig. 4). Thus, this is an obvious target for further studies. Furthermore, since we do not have data coverage on the outermost shelf to shelf edge (Fig. 4), we cannot provide further evidence as to whether the GrIS reached a shelf break position in Norske Trough. Arndt et al. (2017) reported the occurrence of sparse glacial lineations directly at the shelf break on the northern edge of Norske Trough, providing some morphological evidence for grounded ice conditions at this position (Fig. 4). However, north of Norske Trough at 79.4° N (see location in Fig. 1A), the finding of bryozoans/bivalve fragments with $^{14}C$ dates spanning the whole global LGM-early deglaciation (25.5–17.5 cal Kyr BP) may indicate that the GrIS only reached the shelf edge at the main cross-shelf troughs, but not in the areas in between (Rasmussen et al., 2022).

### 5.2. Ice stream dynamics during the last deglaciation

The distribution of glacial landforms in Norske Trough, encompassing transverse wedge and ridge systems, displays, to a large degree, the dynamic retreat of the ice margin during the last deglaciation. These glacial landforms mark different retreat styles and periods of grounding line stabilization during retreat (Figs. 4 and 9A, B).

Moraine ridges on the seafloor of the outer to middle trough indicate that retreat of the Norske Trough ice stream was stepwise with episodes of relatively short grounding line stabilizations, while the presence of two large GZWs (GZW-1 and GZW-2; Fig. 2B–D and 6D, E) demonstrates that the ice stream grounded for a longer time and contributed to the formation of large-scale sediment wedges (Golledge and Phillips, 2008; Ó Cofaigh et al., 2008; Dowdeswell and Fugelli, 2012; Batchelor and Dowdeswell, 2015). Since the formation of recessional moraines and/or GZWs involve a grounded ice stream/glacier margin (e.g., Batchelor and Dowdeswell, 2015), a fast and continuous ice stream retreat from the outer to middle Norske Trough seems unlikely. In contrast, preserved large-scale glacial lineations on the seafloor of the inner trough, originally formed during the ice stream advance (Figs. 4 and 5), suggest a fast-grounding line retreat beyond the recent coastline in order to maintain these former features (Fig. 9B and C). A fast-flowing paleo-ice stream sited on the mid-shelf of Norske Trough has been discussed previously (e.g., Evans et al., 2009; Winkelmann et al., 2010; Arndt et al., 2017). Accordingly, we suggest that the late deglaciation in Norske Trough was first characterized by a phase of stepwise ice retreat punctuated by at least two stillstands followed by a second phase of rapid and continuous grounding line retreat beyond the recent coastline (Figs. 4 and 9). Similar ice retreat dynamics have been reported for other paleo-ice streams in NE Greenland (e.g., at Westwind and Store Koldewey troughs; Arndt et al., 2017; Olsen et al., 2020). In addition, the landform assemblage may indicate the nature of the former ice stream/glacier margin terminus (e.g., Ottesen and Dowdeswell, 2009; Batchelor and Dowdeswell, 2015). In Norske Trough, the interpreted landforms, including low-relief moraines and GZWs (Section 4.3.), aligns with the conceptual model proposed by Batchelor and Dowdeswell (2015). According to this model, the formation of such an

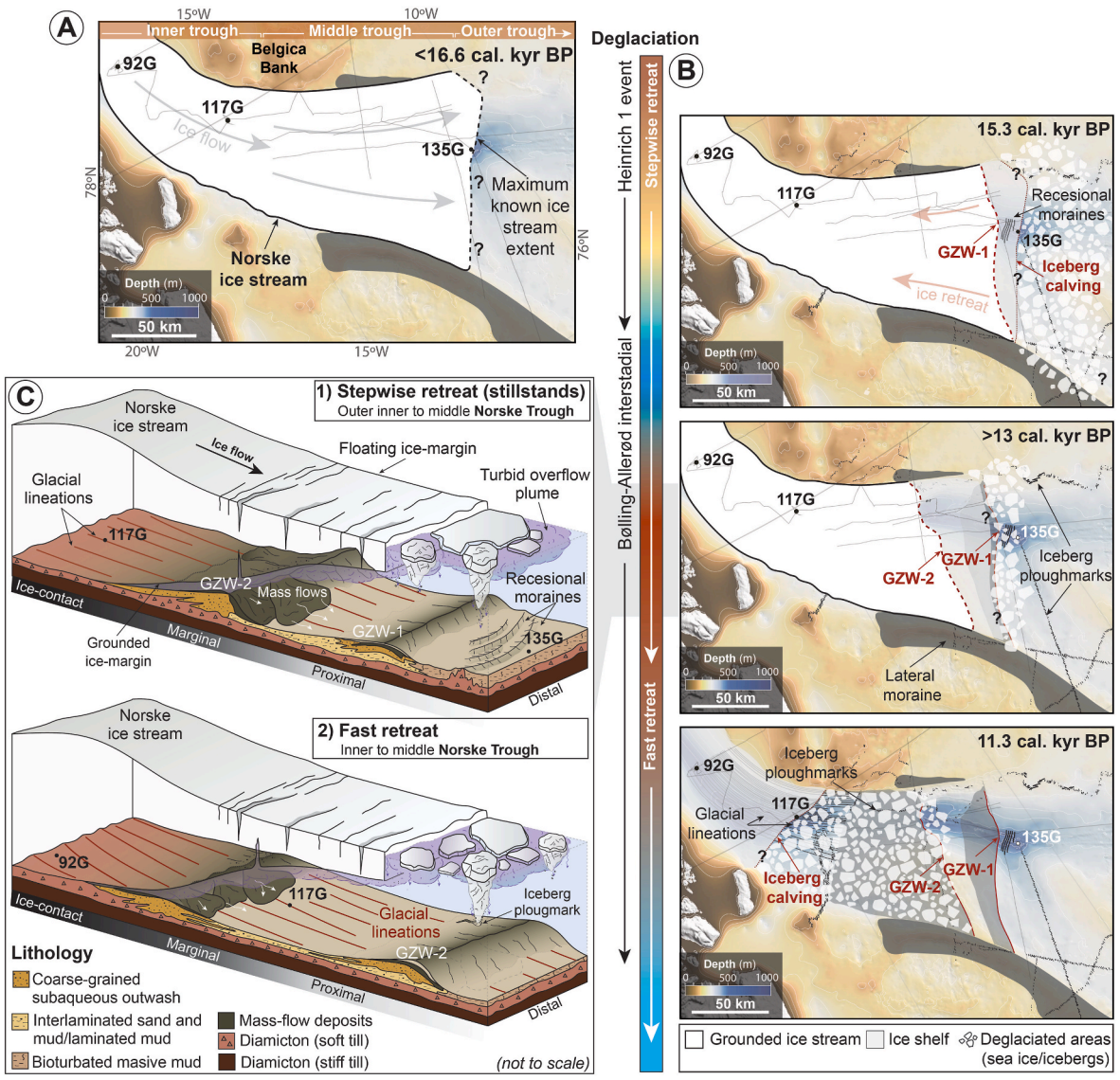


**Fig. 9.** Extent, timing and nature of retreat of the Norske Trough ice stream. A) Reconstruction of the maximum known ice stream extent during the Last Glacial Maximum. B) Reconstruction of the ice stream dynamics during the last deglaciation. Note that the ice margin positions during deglaciation are indicated. Sea ice and icebergs indicate ice rafting and iceberg calving. Stages in A) and B) represent zones defined by the landform assemblage/lithological units interpreted in this work. Detailed distribution of seafloor features in Fig. 4. C) Conceptual model of the landforms/glaciomarine sedimentation associated with (1) a first phase of stepwise retreat with episodes of grounding line stabilizations (formation of GZWs), and (2) a second phase of fast-grounding line retreat. Interpreted lithological units in this work (Fig. 7) were used as a proxy for the relative proximity of ice margin terminus to core sites 92G, 117G, and 135G.

association is preferentially initiated by the presence of ice streams terminating as floating ice shelves. The presence of floating ice sheets in Norske Trough has also been suggested on the basis of benthic foraminiferal assemblages reported from core 92G (Davies et al., 2022). Therefore, the formation of a floating ice shelf margin terminus in Norske Trough during most of its retreat seems reasonable (Fig. 9B) (see below).

These glacial landforms and their spatial distributions could be attributed to the cross-shelf trough morphology, as it has been related in other glaciated continental shelves. Ice streams with landward dipping bed slopes (also referred as 'reverse-bed slopes') have shown fast grounding line retreat (e.g., at Amundsen Sea, including the Pine Island ice stream, in West Antarctica; Jenkins et al., 2010; Smith et al., 2011, 2017). However, observations both in west Antarctica (e.g., at Marguerite Bay; Jamieson et al., 2012) and West Greenland (e.g., at Disko Trought; Hogan et al., 2016) proved that grounding-line stability can be maintained on reverse bed slopes due to increased lateral drag. Lateral constraints on ice flow stabilization have also been discussed in other areas of West Greenland (e.g., at Petermann Fjord and northern Nares Strait; Reilly et al., 2019; Jennings et al., 2022). Norske Trough has a reverse bed slope with 320 m water depth at the shelf break that increases to 560 m on the inner shelf (Arndt et al., 2015, Fig. 1B). In our study area, the mid-shelf GZW (GZW-2) is observed immediately upstream of a converging large-scale glacial lineation field at the inner shelf (Fig. 4), so it is conceivable that funneling of ice as the cross-shelf trough narrowed by ~30 km may have led to increased lateral drag and subsequently grounding-line stability. Moreover, if a former topographic high was present on the middle shelf, this could have acted as a lateral pinning point for ice stabilization (Jamieson et al., 2012). In the middle Norske Trough, the topography beneath GZW-2, which we interpret as a possible buried pre-LGM GZW (Fig. 2B and C), provides evidence for such a topographically-controlled scenario. Accordingly, shorter periods of ice stability between GZWs may have been related to a gradually grounding line decoupling from the bed as the ice margin

retreated across deeper water, while the ice front again became grounded and stable at topographic highs. Once the grounding line again encountered water depths of less than ~460–560 m (i.e., the landward boundary of the mid-shelf GZW-2; Fig. 4), a threshold was likely reached on the reverse bed slopes of Norske Trough. Such a threshold is reinforced by the lack of ice marginal landforms throughout the inner shelf. After the threshold was reached, increased grounding line instability on the reverse bed slopes may have locally exacerbated ice retreat. Therefore, inferred initial stepwise retreat at Norske Trough can be linked to the exerted cross-shelf trough geometry (Fig. 9), which is also in line with numerical simulations of ice sheet grounding line dynamics (Schoof, 2007).

The sedimentary sequence starting with a basal till (LU-VII) overlain by glaciomarine (LU-VI to LU-II) deposits demonstrates the transition from subglacial to a grounding-zone proximal setting and then, to a proximal to distal glaciomarine environment characterized by suspension settling from meltwater plumes and iceberg rain-out. A change to a fully open marine environment is recorded at the upper sedimentary sequence, characterized mainly by hemipelagic sedimentation (LU-I). Vertical stacking patterns and proximal-to-distal variations in the deglacial depositional architecture are also considered (Figs. 3, 7 and 9). Radiocarbon dates from glaciomarine sediments in our sediment cores constrain the timing of ice retreat across Norske Trough (Fig. 7). The earliest date of marine inundation, following glacier retreat, is from core 135G from the outer trough in front of a moraine/GZW (GZW-1) system (Fig. 4). Laminated muds, with occasional IRD, from the base of the glaciomarine record (LU-V) dated 16.6 cal Kyr BP; this shows that the outer shelf was ice-free by that time (Fig. 9B). This is significantly earlier than the date of 15.5 to 12.3 cal Kyr BP accepted for initial retreat of the inner/middle shelf in NE Greenland; though this estimate is based on a limited number of offshore age constraints (see review by Larsen et al., 2022, and references therein). In core 135G, deposition of laminated muds with occasional IRD (LU-V) is related to suspension settling from meltwater plumes in a grounding line proximal setting until 16.17 cal Kyr BP. Although the exact timing of GZW-1 formation is uncertain, the formation of GZWs include the stabilization of the ice margin for decades to centuries (e.g., Dowdeswell and Fugelli, 2012). In Norske Trough, grounding line stabilization at the outer-shelf GZW (GZW-1) therefore likely lasted 500 cal Yr BP in line with sediment stacking of deposited laminated muds in core 135G (Fig. 7). The timing of ice retreat and following grounding-line stabilization at the GZW-1 further coincides with the Heinrich Stadial 1 that led to a period of (sub)surface ocean warming associated with declining Atlantic meridional overturning circulation (AMOC) between 18 and ~15 cal Kyr BP (e.g., Hulbe et al., 2004; Rasmussen and Thomsen, 2004, 2021; Marcott et al., 2011; Hodell et al., 2017; Bassis et al., 2017). Overlying laminated muds, a 20-cm-thick matrix-supported diamictic interval (LU-IV) is interpreted, as proposed for Antarctic sub-ice shelf lithofacies (Smith et al., 2019), to have been deposited in an ice-proximal glaciomarine environment by vigorous iceberg rafting as the calving zone of a floating ice shelf passed over site 135G between 15.3 and 12.9 cal Kyr BP (Fig. 9B). This IRD-rich lithological unit thus suggests the presence of an extensive ice shelf in Norske Trough. On the basis of seafloor features, Arndt et al. (2017) also suggested the presence of a thick ice shelf in Norske Trough releasing tabular icebergs. The timing of major calving front instability, likely derived from the outer-shelf GZW-1 (Fig. 9B), coincides with the Bølling-Allerød interstadial that led to different well-known atmospheric warming phases and massive intrusions of warm Atlantic Water beneath Polar surface waters along the Svalbard margin-Fram Strait and regionally (e.g., Rasmussen et al., 2007; Slubowska-Woldengen et al., 2007; Aagaard-Sørensen et al., 2014; Consolaro et al., 2018; Hansen et al., 2022).

As discussed before, GZW-2 marks a major grounding line position on the middle shelf of Norske Trough. However, the timing of this GZW formation remains unclear. Previous discussions suggest that GZW-2 was formed by a re-advance of the GrIS during the Younger Dryas (Arndt et al., 2017). In contrast, our combined dataset and radiocarbon ages indicate that re-advance during the Younger Dryas is unlikely. This aligns with a recent re-investigation of deglacial ice margin features in Greenland, which were formerly attributed to Younger Dryas ice margin readvances, and which was subsequently shown to not be linked to the Younger Dryas (Funder et al., 2021 and references therein). Moreover, none of the recent $^{14}$C- and $^{10}$Be-dated records provide evidence for ice margin response to the initial Younger Dryas cooling (Fig. 4 in Funder et al., 2021). At the western side of the mid-shelf GZW-2 (Fig. 4), radiocarbon dates from deglacial sediments (laminated muds of LU-V; cores 117G and 92G; Fig. 7) demonstrate that much of the shelf in Norske Trough was free from grounded ice by and likely before 12.5 cal Kyr BP (Figs. 7 and 9B) (Lloyd et al., 2023). As in core 135G, laminated muds (LU-V) in cores 117G and 92G are related to suspension settling from meltwater discharges possibly below a floating ice shelf, while deposition of overlying LU-IV (matrix-supported iceberg rafted diamicton) in core 117G indicate that the calving front of a floating ice shelf passed over this site location at 11.3 cal Kyr BP in the early Holocene (Fig. 9B). Therefore, because there is no evidence of a significant readvance of the ice stream onto the continental shelf during the Younger Dryas, a widespread floating ice shelf with vigorous sea-ice and/or iceberg rafting production occupied the inner Norske Trough (Fig. 9B).

On NE Greenland shelf, evidence of relatively warm water from the North Atlantic Ocean, advected into the Fram Strait, is reported for the initial phase of deglaciation (19.5–14.5 cal Kyr BP; Hebbeln et al., 1994). Recent studies also reported evidence of a strong inflow of Atlantic Water beneath Polar surface waters between 14.1 and 12.9 cal Kyr BP; e.g., on the western Svalbard margin, eastern Fram Strait (e.g., Rasmussen et al., 2007; Slubowska-Woldengen et al., 2007; Aagaard-Sørensen et al., 2014), in the deeper eastern Fram Strait (e.g., Consolaro et al., 2018), and on NE Greenland shelf in the western Fram Strait (e.g., Davies et al., 2022; Rasmussen et al., 2022; Hansen et al., 2022; Jackson et al., 2022). Similarly, an increasing inflow of (sub) surface Atlantic Water was reported during the Bølling-Allerød on the SE Greenland shelf (e.g., Stein et al., 1996; Jennings et al., 2006). This indicates that the timing of warm Atlantic water inflow to Fram Strait matches with the initial phase of deglaciation from 19.5 to ~15 to 14.7–12.9 cal Kyr BP. It is therefore plausible that the intrusion of warm Atlantic Water through the deep troughs of the NE Greenland shelf and caused enhanced basal melting of the ice along the reversed bed slopes of Norske Trough; ultimately triggering the initial stepwise retreat/iceberg discharge before 16.6 cal Kyr BP. Furthermore, increasing inflow of Atlantic Water during the Bølling-Allerød likely triggered fast ice retreat in Norske Trough (Fig. 9B). Today, an analogous setting with initial stepwise ice retreat along a reverse sloped bed at the grounding line is reported in West Antarctica, beneath Pine Island Glacier. Here, relatively warm Circumpolar Deep Water is upwelling onto the shelf, following the cross-shelf troughs towards the main glacier cavity, where it triggers basal melting and thus a fast-grounding line retreat (Jenkins et al., 2010; Smith et al., 2011, 2017). The climatic and oceanographic variations associated with both Heinrich Stadial 1 and the Bølling-Allerød interstadial are thus potential external forcing mechanisms on ice stream dynamics in Norske Trough. The GZWs and smaller transverse recessional moraines that we document across the outer-to mid-shelf point to stillstands interrupting the overall ice retreat (Fig. 9B). Hence, it is most likely that the pre-existing shelf geometry in Norske Trough was also an important controlling factor triggering initial stepwise ice retreat.

### 5.3. Postglacial development

Postglacial sedimentary processes in Norske Trough are interpreted to comprise terrigenous pelagic settling to hemipelagic deposition (LU-III to LU-II) to mostly hemipelagic sedimentation (LU-I), indicating a change from ice-distal glaciomarine to fully open marine environments (Fig. 7). The low occurrence of IRD from LU-III to LU-I also suggest a

limited contribution from iceberg and/or sea-ice rafting during sediment deposition. This may indicate that Norske Trough ice stream had fully retreated onto land during the early Holocene (Bennike and Björck, 2002). However, deposition of bioturbated foraminifera-bearing muds (LU-III) with high concentrations of IRD in core 92G support the previous suggestion by Davies et al. (2022) of a return to ice-proximal glaciomarine conditions, accompanied by the reformation of the ice shelf on the innermost trough from 10.8 to 9.6 cal Kyr BP. This period correlates with the onset of maximum Atlantic advection at both subsurface and surface depths in the eastern Fram Strait (e.g., Werner et al., 2016) and the dominance of colder subsurface water conditions on the NE Greenland shelf, with sustained influx of Atlantic Water flowing beneath (Syring et al., 2020; Davies et al., 2022; Hansen et al., 2022; Rasmussen et al., 2022). Debris particles entrapped in icebergs calving off from this reformed ice shelf may have melted out quickly so that icebergs rarely reached the middle to outer shelf of Norske Trough during the early Holocene.

After a brief return to ice-proximal conditions on the innermost shelf, the depicted increase in burrowing activity in LU-III, between 9.6 and 7.9 cal Kyr BP (Figs. 7 and 8 M, N), may again indicate a shift to a more distal proglacial environment as the ice shelf fully break up and the ice margin retreated on land. In core 92G, the dominance of Atlantic Water foraminiferal species until 7.9 cal Kyr BP (Davies et al., 2022), confirms the presence and influence of a subsurface warm water signal along Norske Trough, and that it may have played a role in the total disintegration of the ice shelf. This coincides with the early Holocene Climatic Optimum (dated 9.5–7 cal Kyr BP; Johnsen et al., 2001; Vinther et al., 2009) when temperatures in NE Greenland were 2–3 °C warmer than present-day values (Fréchette and de Vernal, 2009; Klug et al., 2009; Axford et al., 2013). It is proposed that this shift towards warmer conditions probably forced the 79°-Glacier and Zachariae Isstrøm ice margin to retreat behind its modern ice extent (Fig. 1B) (Syring et al., 2020; Davies et al., 2022). This is supported by recently dated mollusks from raised marine deposits around Blåsø Lake (Smith et al., 2023), a large epishelf lake located 2–13 km from the present grounding line of 79°-Glacier (Fig. 1B), confirming that the 79°-Glacier ice shelf was ~70 km inland of the present ice shelf margin between ~8.5 and 4.4 cal Kyr BP. In addition, sea-ice formation on the NE Greenland shelf and the Arctic Ocean was reduced during this period (e.g., Funder et al., 2011; Müller et al., 2012; Werner et al., 2016; Syring et al., 2020). Accordingly, a rise in ocean temperatures may have triggered the deposition of postglacial, mostly hemipelagic sediments of late LU-III in Norske Trough.

Although uncertain, bioturbated massive clayey muds (LU-II) overlain by bioturbated massive muds (LU-I) deposited during the mid to late Holocene are present, spanning the past ~7.9 cal Kyr B (Fig. 7). Our proxy data in cores 135G and 117G suggest that bioturbated clayey muds (LU-II) deposited in the outer to inner shelf under conditions of enhanced productivity in open marine waters (Figs. 7 and 8O). This is also supported by the presence of some productivity-indicator foraminiferal species at the bottom of LU-II in core 92G (at ~7.9 cal Kyr BP; Davies et al., 2022). However, differences in depositional sediment conditions characterize the innermost shelf of Norske Trough. In core 92G, a drop in sedimentation rates was evidenced during the mid to late Holocene (Davies et al., 2022). Similarly, a reduced sediment flux from land at 7.5 cal Kyr BP was recorded in core PS100/270, located 130 km northwest of core 92G (Fig. 1B) (Syring et al., 2020). This reduction in sediment accumulation rates has been linked to an increase in perennial sea ice cover (Davies et al., 2022; Syring et al., 2020). Accordingly, Norske Trough may have experienced an increase in surface water productivity after 7.9 cal Kyr BP, except on the innermost shelf where sea ice cover most likely triggered water stratification limiting marine primary production.

Late Holocene sediments of LU-I may indicate deposition in an open marine environment with short term fluctuations in sea ice/ocean primary production. However, the significance and precise timing of sedimentary processes recorded in the uppermost sedimentary sequence require further work.

## 6. Conclusions

By integrating conventional 2D and high-resolution seismic data with multi-proxy analyses of sediment gravity cores from Norske Trough, the timing and dynamics of ice retreat after the LGM have been reconstructed and conceptually illustrated in Fig. 9.

- During the LGM, a fast-flowing ice stream advanced to the outer shelf in Norske Trough. The presence of glacial lineations extending almost to a complex outer-shelf GZW/moraine system, and subglacial till cored at the outer trough, confirm that grounded ice extended to this shelf position. The grounded ice possibly originated from the areas at present mostly occupied by the floating ice tongue of the 79°-Glacier and the Jøkelbugten fjord, in which the Zachariae Isstrøm drains.
- Initial retreat was underway before 16.6 cal Kyr BP, significantly earlier than previously known for this sector of the NE Greenland shelf. Recessional moraines and GZWs on the seafloor of the outer to middle shelf indicate that initial retreat was episodic, punctuated by stillstands. The outer-shelf GZW (GZW-1) marks the first known grounding line position in Norske Trough by, and likely after, 15.3 cal Kyr BP. The last grounding line position is recorded by the establishment of a major GZW (GZW-2) at the middle shelf before 13 cal Kyr BP. In contrast, preserved, large-scale glacial lineations on the seafloor of the inner shelf indicate that retreat from the inner trough to the coastline was rapid.
- The lithostratigraphy of the uppermost trough strata includes subglacial till covered with a drape of up to 37 m thick ice-proximal to distal glaciomarine/hemipelagic sediments. Retreat occurred in a glaciomarine setting and the ice sheet terminated mostly in a floating ice shelf.
- The results underscore the importance of former shelf geometry, fostering pinning points for grounding-zone stabilization during ice retreat through increased drag and reduced mass flow across the grounding zone. In Norske Trough, pre-LGM shelf geometry played an important role fostering pining points.
- The shelf was free from grounded ice by, and likely before 12.5 cal Kyr BP. There is no evidence of grounded-ice re-advances during the Younger Dryas, although a floating ice shelf with vigorous sea-ice and iceberg rafting production occupied the inner trough at 11.3 cal Kyr BP.
- $^{14}C$ dates revealed that pre-Holocene, initial stepwise ice retreat followed by fast retreat coincide with two abrupt climatic events (the Heinrich Stadial 1 and the Bølling-Allerød interstadial, respectively) linked with inflows of warm Atlantic Water, indicating a strong ocean/climate control on the late deglaciation of Norske Trough.
- Postglacial (Holocene) depositional processes were mainly driven by pelagic settling to hemipelagic sedimentation, evidencing a transition from an ice-distal glaciomarine to open marine environments. From 10.8 to 9.6 cal Kyr BP, a shift in ocean circulation resulted in a renewal of ice-proximal conditions and reformation of the ice shelf in the innermost trough. After 9.6 cal Kyr BP, the ice shelf fully broke up in Norske Trough. The mid to late Holocene record was likely characterized by short-term fluctuations in sea ice production and variations in ocean productivity.

## Financial support

Funding for this research was provided by the Independent Research Fund Denmark (grant no. 0135–00165 B (GreenShelf project)). The cruise was funding by the Danish Centre for Marine Research, the Engineering Research Council of Canada, and the Independent Research Fund Denmark (G-Ice Project (grant no. 7014-00113 B/FNU). A.L.-Q.

also thanks the Spanish Ministry of Science and Innovation (MCIN) for Research Contract FJC 2021-047046-I (MCIN/AEI/10.13039/501100011033 and NextGenerationEU/PRTR).

## CRediT authorship contribution statement

**Adrián López-Quirós:** Conceptualization, Formal analysis, Writing – original draft, Writing – review & editing, Visualization, Project Management. **Tuomas Junna:** Formal analysis. **Joanna Davies:** Formal analysis, Writing – review & editing. **Katrine J. Andresen:** Visualization, Data Acquisition - NorthGreen2017 cruise, Data curation, Formal analysis, Writing – review & editing. **Tove Nielsen:** Data Acquisition - NorthGreen2017 cruise, Formal analysis, Writing – review & editing. **Negar Haghipour:** Formal analysis. **Lukas Wacker:** Formal analysis, Writing – review & editing. **Aage Kristian Olsen Alstrup:** Formal analysis. **Ole Lajord Munk:** Formal analysis. **Tine L. Rasmussen:** Data Acquisition - NorthGreen2017 cruise, Writing – review & editing. **Christof Pearce:** Resources, Visualization, Data Acquisition - NorthGreen2017 cruise, Data curation, Writing – review & editing. **Marit-Solveig Seidenkrantz:** Project management, Conceptualization, Funding acquisition, Resources, Cruise planning, and Leading, Data Acquisition - NorthGreen2017 cruise, Data curation, Writing – review & editing.

## Declaration of competing interest

The authors declare that they have no known competing financial interests or personal relationships that could have appeared to influence the work reported in this paper.

## Data availability

Data for this research is available here and in the supplementary data to this article. Additional data will be made available on request.

## Acknowledgments

We thank the captain, officers, crew, and scientific staff onboard the NorthGreen2017 cruise with R/V Dana for their support in obtaining the data, sometimes under severe sea conditions. We also thank Dr. Anne de Vernal, who acquired part of the funding for the cruise. We acknowledge the help of Trine Ravn-Jonsen (Department of Geoscience, Aarhus University) for running and composing the XRF dataset. We would also thank Dr. Rocío Marquez Crespo (Scientific Instrumentation Center, University of Granada) for her assistance using the FESEM. S&P Global is thanked for providing academic licenses for SeisLab Aarhus for use of the Kingdom seismic interpretation software. We are also grateful to TGS-NOPEC Geophysical Company ASA for providing 2D multichannel seismic reflection data. We also appreciate the constructive comments provided by Editor Giovanni Zanchetta and anonymous reviewers that greatly improved the manuscript.

## Appendix A. Supplementary data

Supplementary data to this article can be found online at https://doi.org/10.1016/j.quascirev.2023.108477.

## References

Aagaard Sørensen, S., Husum, K., Werner, K., Spielhagen, R.F., Hald, M., Marchitto, T.M., 2014. A late glacial-early Holocene multiproxy record from the eastern Fram Strait, polar North Atlantic. Mar. Geol. 355, 15–26.

Anderson, J.B., 1999. Antarctic Marine Geology. Cambridge University Press, London, UK.

Anderson, J.B., Kurtz, D.D., Domack, E.W., Balshaw, K.M., 1980. Glacial and glacial marine sediments of the Antarctic continental shelf. J. Geol. 88, 399–414.

Andreassen, K., Winsborrow, M.C.M., Bjarnadóttir, L.R., Rüther, D.C., 2014. Ice stream retreat dynamics inferred from an assemblage of landforms in the northern Barents Sea. Quat. Sci. Rev. 92, 246–257.

Arndt, J.E., 2018. Marine geomorphological record of ice sheet development in east Greenland since the last glacial maximum. J. Quat. Sci. 33, 853–864.

Arndt, J.E., Jokat, W., Dorschel, B., 2017. The last glaciation and deglaciation of the Northeast Greenland continental shelf revealed by hydro-acoustic data. Quat. Sci. Rev. 160, 45–56.

Arndt, J.E., Jokat, W., Myklebust, J.A., Dowdeswell, A., Evans, J., 2015. A new bathymetry of the Northeast Greenland continental shelf: constraints on glacial and other processes. G-cubed 16, 3733–3753.

Axford, Y., Losee, S., Briner, J.P., Francis, D.R., Langdon, P.G., Walker, I.R., 2013. Holocene temperature history at the western Greenland Ice Sheet margin reconstructed from lake sediments. Quat. Sci. Rev. 59, 87–100.

Bamber, J.L., Griggs, J.A., Hurkmans, R.T.W.L., Dowdeswell, J.A., Gogineni, S.P., Howat, I., Mouginot, J., Paden, J., Palmer, S., Rignot, E., Steinhage, D., 2013. A new bed elevation dataset for Greenland. Cryosphere 7, 499–510.

Bamber, J.L., Oppenheimer, M., Kopp, R.E., Aspinall, W.P., Cooke, R.M., 2019. Ice sheet contributions to future sea-level rise from structured expert judgment. Proc. Natl. Acad. Sci. U.S.A. 116, 11195–11200.

Bard, E., Tuna, T., Fagault, Y., Bonvalot, L., Wacker, L., Fahrni, S., Synal, H.A., 2015. AixMICADAS, the accelerator mass spectrometer dedicated to $^{14}C$ recently installed in Aix-en-Provence, France. Nucl. Instrum. Methods Phys. Res. Sect. B Beam Interact. Mater. Atoms 361, 80–86.

Bassis, J.N., Petersen, S.V., Mac Cathles, L., 2017. Heinrich events triggered by ocean forcing and modulated by isostatic adjustment. Nature 542, 332–334.

Batchelor, C.L., Dowdeswell, J.A., 2015. Ice-sheet grounding-zone wedges (GZWs) on high-latitude continental margins. Mar. Geol. 363, 65–92.

Batchelor, C.L., Dowdeswell, J.A., 2014. The physiography of High Arctic cross-shelf troughs. Quat. Sci. Rev. 92, 68–96.

Bennike, O., Björck, S., 2002. Chronology of the last recession of the Greenland ice sheet. J. Quat. Sci. 17, 211–219.

Bentley, M.J., Smith, J.A., Jamieson, S.S.R., Lindeman, M.R., Rea, B.R., Humbert, A., Lane, T.P., Darvill, C.M., Lloyd, J.M., Straneo, F., Helm, V., Roberts, D.H., 2023. Direct measurement of warm Atlantic Intermediate Water close to the grounding line of Nioghalvfjerdsfjorden (79° N) Glacier, northeast Greenland. Cryosphere 17, 1821–1837.

Berger, D., Jokat, W., 2008. A seismic study along the East Greenland margin from 72°N to 77°N. Geophys. J. Int. 174 (2), 733–748.

Berger, D., Jokat, W., 2009. Sediment deposition in the northern basins of the North Atlantic and characteristic variations in shelf sedimentation along the East Greenland margin. Mar. Petrol. Geol. 26 (8), 1321–1331.

Bertram, R.A., Wilson, D.J., van de Flierdt, T., McKay, R.M., Jimenez-Espejo, F.J., Escutia, C., Duke, G., Taylor-Silva, B., Riesselman, C., 2018. Timescales and event sequences of middle to late Pliocene deglaciations in the Wilkes Subglacial Basin. Earth Planet Sci. Lett. 494, 109–116.

Blanchet, C.L., Thouveny, N., Vidal, L., 2009. Formation and preservation of greigite ($Fe_3S_4$) in sediments from the Santa Barbara Basin: implication for paleoenvironmental changes during the past 35 ka. Paleoceanography 24, PA2224.

Bond, G.C., Lotti, R., 1995. Iceberg discharges into the North Atlantic on millennial time scales during the last glaciation. Science 267 (5200), 1005.

Bourke, R.H., Newton, J.L., Paquette, R.G., Tunnicliffe, M.D., 1987. Circulation and water masses of the East Greenland shelf. J. Geophys. Res. Ocean. 92, 6723–6740.

Burdige, D.J., 1993. The biogeochemistry of manganese and iron reduction in marine sediments. Earth Sci. Rev. 35, 249–284.

Cage, A.G., Pieńkowski, A.J., Jennings, A., Knudsen, K.L., Seidenkrantz, M.-S., 2021. Comparative analysis of six common foraminiferal species of the genera *Cassidulina*, *Paracassidulina* and *Islandiella* from the Arctic-North Atlantic domain. J. Micropalaeontol. 40, 37–60.

Callard, S.L., Ó Cofaigh, C., Benetti, S., Chiverrell, R.C., Van Landeghem, K.J.J., Saher, M. H., Livingstone, S.J., Clark, C.D., Small, D., Fabel, D., Moreton, S.G., 2020. Oscillating retreat of the last British-Irish Ice Sheet on the continental shelf offshore Galway Bay, western Ireland. Mar. Geol. 420, 106087.

Canals, M.R., Urgeles, R., Calafat, A.M., 2000. Deep sea-floor evidence of past ice streams off the Antarctic Peninsula. Geology 28, 31–34.

Chawchai, S., Kylander, M.E., Chabangborn, A., Lowemark, L., Wohlfarth, B., 2016. Testing commonly used X-ray fluorescence core scanning-based proxies for organic rich lake sediments and peat. Boreas 45 (1), 180–189.

Choi, Y., Morlighem, N., Rignot, E., Mouginot, J., Wood, M., 2017. Modeling the response of nioghalvfjerdsfjorden and Zachariae Isstrøm glaciers, Greenland, to ocean forcing over the next century. Geophys. Res. Lett. 44 (21), 11,0171-11,079.

Church, J.A., Clark, P.U., Cazenave, A., Gregory, J.M., Jevrejeva, S., Levermann, A., Merrifield, M.A., Milne, G.A., Nerem, R.S., Nunn, P.D., Payne, A.J., Pfeffer, W.T., Stammer, D., Unnikrishnan, A.S., 2013. Sea level change. In: Stocker, T.F., Qin, D., Plattner, G.-K., Tignor, M., Allen, S.K., Boschung, J., Nauels, A., Xia, Y., Bex, V., Midgley, P.M. (Eds.), Climate Change 2013: the Physical Science Basis. Contribution of Working Group I to the Fifth Assessment Report of the Intergovernmental Panel on Climate Change. Cambridge University Press, Cambridge, United Kingdom and New York, NY, USA.

Clark, P.U., Dyke, A.S., Shakrun, J.D., Carlson, A.E., Clark, J., Wohlfarth, B., Mitrovica, J. X., Hostetler, S.W., McCabe, A.M., 2009. The last glacial maximum. Science 325, 710–714.

Clark, P.U., Mix, A.C., 2002. Ice sheets and sea level of the last glacial maximum. Quat. Sci. Rev. 21, 1–7.

Consolaro, C., Rasmussen, T.L., Panieri, G., 2018. Palaeoceanographic and environmental changes in the eastern Fram Strait during the last 14,000years based on benthic and planktonic foraminifera. Mar. Micropaleontol. 139, 84–101.
Croudace, I.W., Rindby, A., Rothwell, R.G., 2006. ITRAX: description and evaluation of a new multi-function X-ray core scanner. Geol. Soc. London, Spec. Publ. 267, 51–63.
Davies, J., Mathiasen, A.M., Kristiansen, K., Hansen, K.E., Wacker, L., Alstrup, A.K.O., Munk, O.L., Pearce, C., Seidenkrantz, M.-S., 2022. Linkages between ocean circulation and the Northeast Greenland ice stream in the Early Holocene. Quat. Sci. Rev. 286, 107530.
Dawes, P.R., 2009. The bedrock geology under the Inland Ice: the next major challenge for Greenland mapping. GEUS Bull. 17, 57–60.
de Steur, L., Hansen, E., Gerdes, R., Karcher, M., Farbach, E., Holfort, J., 2009. Freshwater fluxes in the East Greenland current: a decade of observations. Geophys. Res. Lett. 36, L23611.
Diekmann, B., Hofmann, J., Henrich, R., Fütterer, D.K., Röhl, U., Wei, K.-Y., 2008. Detrital sediment supply in the southern Okinawa Trough and its relation to sea level and Kurishio dynamics during the late Quaternary. Mar. Geol. 255, 83–95.
Domack, E.W., Jacobson, E.A., Shipp, S., Anderson, J.B., 1999. Late pleistocene–holocene retreat of the west antarctic ice-sheet system in the ross sea: Part 2— sedimentologic and stratigraphic signature. Geol. Soc. Am. Bull. 111, 1517–1536.
Døssing, A., Japsen, P., Watts, A.B., Nielsen, T., Jokat, W., Thybo, H., Dahl-Jensen, T., 2016. Miocene uplift of the NE Greenland margin linked to platetectonics: seismic evidence from the Greenland Fracture Zone, NE Atlantic. Tectonics 35, 257–282.
Dowdeswell, J.A., Bamber, J.L., 2007. Keel depths of modem Antarctic icebergs and implications for sea-floor scouring in the geological record. Mar. Geol. 243, 120–131.
Dowdeswell, J.A., Villinger, H., Whittinton, R.J., Marienfeld, P., 1993. Iceberg scouring in scoresby Sund and on the east Greenland continental shelf. Mar. Geol. 111, 37–53.
Dowdeswell, J.A., Fugelli, E.M.G., 2012. The seismic architecture and geometry of grounding-zone wedges formed at the marine margins of past ice sheets. Geol. Soc. Am. Bull. 124 (11/12), 1750–1761.
Dowdeswell, J.A., Ó Cofaigh, C., Pudsey, C.J., 2004. Thickness and extent of the subglacial till layer beneath an Antarctic paleo–ice stream. Geology 32 (1), 13–16.
Dowdeswell, J.A., Ottesen, D., Evans, J., Ó Cofaigh, C., Anderson, J.B., 2008. Submarine glacial landforms and rates of ice-stream collapse. Geology 36, 819–822.
Dreimanis, A., Vagners, U.J., 1971. Bimodal distribution of rock and mineral fragments in basal tills. In: Goldthwait (Ed.), Till, a Symposium, 237–250. Ohio State University Press.
Dymond, J., Suess, E., Lyle, M., 1992. Barium in deep-sea sediment: a geochemical proxy for paleoproductivity. Paleoceanography 7, 163–181.
Evangelinos, D., Escutia, C., Etourneau, J., Hoem, F., Bijl, P., Boterblom, W., van de Flierdt, T., Valero, L., Flores, J.-A., Rodriguez-Tovar, F.J., Jimenez-Espejo, F.J., Salabarnada, A., López-Quirós, A., 2020. Late oligocene- Miocene proto-antarctic circumpolar current dynamics off the wilkes land margin, east Antarctica. Global Planet. Change 191, 103221.
Evans, D.J.A., 2018. Till: a Glacial Process Sedimentology. Wiley Blackwell, Chichester.
Evans, D.J.A., Phillips, E.R., Hiemstra, J.F., Auton, C.A., 2006. Subglacial till: formation, sedimentary characteristics and classification. Earth Sci. Rev. 78 (1–2), 115–176.
Evans, J., Dowdeswell, J.A., Grobe, H., Niessen, F., Stein, R., Hubberten, H., Whittington, R.J., 2002. Late quaternary sedimentation in kejser Franz joseph fjord and the continental margin of east Greenland. pp149-180. In: Dowdeswell, J.A., Ó Cofaigh, C. (Eds.), Glacier-influenced Sedimentation on High-Latitude Continental Margins. Geological Society of London, London.
Evans, J., Ó Cofaigh, C., Dowdeswell, J.A., Wadhams, P., 2009. Marine geophysical evidence for former expansion and flow of the Greenland Ice Sheet across the north-east Greenland continental shelf. J. Quat. Sci. 24, 279–293.
Evans, J., Pudsey, C.J., 2002. Sedimentation associated with Antarctic Peninsula ice shelves: implications for palaeoenvironmental reconstructions of glacimarine sediments. J. Geol. Soc. 159, 233–237.
Fleming, K., Lambeck, K., 2004. Constraints on the Greenland ice sheet since the last glacial maximum from sea-level observations and glacial-rebound models. Quat. Sci. Rev. 23, 1053–1077.
Folk, R.L., 1954. The distinction between grain size and mineral composition in sedimentary-rock nomenclature. J. Geol. 62 (4), 344–359.
Forwick, M., Vorren, T.O., 2009. Late Weichselian and Holocene sedimentary environments and ice rafting in Isfjorden. Spitsbergen. Palaeogeography, Palaeoclimatology, Palaeoecology. 280, 258–274.
Fréchette, B., de Vernal, A., 2009. Relationship between Holocene climate variations over southern Greenland and eastern Baffin Island and synoptic circulation pattern. Clim. Past 5, 347–359.
Funder, S., 1982. $^{14}$C-dating of samples collected during the 1979 expedition to North Greenland. Rapp. GrØnlands geol. Unders. 110, 9–14.
Funder, S., Kjeldsen, K.K., Kjær, K.H., O Cofaigh, C., 2011. The Greenland Ice Sheet during the past 300,000 years: a review. In: Ehlers, J., Gibbard, P., Hughes, P. (Eds.), Quaternary Glaciations - Extent and Chronology, Part IV: A Closer Look. Elsevier, pp. 699–713.
Funder, S., Sørensen, A.H.L., Larsen, N.K., Bjørk, A.A., Briner, J.P., Olsen, J., Schomacker, A., Levy, L.B., Kjær, K.H., 2021. Younger Dryas ice margin retreat in Greenland: new evidence from southwestern Greenland. Clim. Past 17, 587–601.
Fürst, J.J., Goelzer, H., Huybrechts, P., 2015. Ice-dynamic projections of the Greenland ice sheet in response to atmospheric and oceanic warming. Cryosphere 9, 1039–1062.
García, M., Dowdeswell, J.A., Ercilla, G., Jakobsson, M., 2012. Recent glacially influenced sedimentary processes on the East Greenland continental slope and deep Greenland Basin. Quat. Sci. Rev. 49, 64–81.
Gilbert, R., Aitken, A.E., Lemmen, D.S., 1993. The glacimarine sedimentary environment of expedition fiord, Canadian high arctic. Mar. Geol. 110, 257–273.
Gjelstrup, C.V.B., Sejr, M.K., de Steur, L., Christiansen, J.S., Granskog, M.A., Koch, B.P., Møller, E.F., Winding, M.H.S., Stedmon, C.A., 2022. Vertical redistribution of principle water masses on the Northeast Greenland Shelf. Nat. Commun. 13, 7660.
Golledge, N., Phillips, E., 2008. Sedimentology and architecture of De Geer moraines in the western Scottish Highlands, and implications for grounding-line glacier dynamics. Sediment. Geol. 208, 1–14.
Grobe, H., 1987. A simple method for the determination of ice-rafted debris in sediment cores. Polarforschung 57, 123–126.
Håkansson, S., 1973. University of Lund radiocarbon dates VI. Radiocarbon 15 (3), 493–513.
Hald, M., Korsun, S., 1997. Distribution of modern benthic foraminifera from fjords of Svalbard, European Arctic. J. Foraminifer. Res. 27, 101–122.
Haldorsen, S., 1981. Grain-size distribution of subglacial till and its relation to glacial crushing and abrasion. Boreas 10, 91–107.
Hamann, N.E., Whittaker, R.C., Stemmerik, L., 2005. Geological development of the northeast Greenland shelf. Pet. Geol. Conf. Ser. 6, 887–902.
Hansen, K.E., Lorenzen, J., Davies, J., Wacker, L., Pearce, C., Seidenkrantz, M.-S., 2022. Deglacial to mid holocene environmental conditions on the northeastern Greenland shelf, western Fram Strait. Quat. Sci. Rev. 293, 107704.
Heaton, T.J., Köhler, P., Butzin, M., Bard, E., Reimer, R.W., Austin, W.E.N., Bronk Ramsey, C., Grootes, P.M., Hughes, K.A., Kromer, B., Reimer, P.J., Adkins, J., Burke, A., Cook, M.S., Olsen, J., Skinner, L.C., 2020. Marine20 - the marine radiocarbon age calibration curve (0-55,000 cal BP). Radiocarbon 62 (4), 779–820.
Hebbeln, D., Dokken, T., Andersen, E.S., Hald, M., Elverhøi, A., 1994. Moisture supply for northern ice-sheet growth during the Last Glacial Maximum. Nature 370, 357–360.
Hebbeln, D., Knudsen, K.-L., Gyllencreutz, R., Kristensen, P., Klitgaard-Kristensen, D., Backman, J., Scheurle, C., Jiang, H., Gil, I., Smelror, M., Jones, P.D., Sejrup, H.P., 2006. Late Holocene coastal hydrographic and climate changes in the eastern North Sea. Holocene 16, 987–1001.
Henriksen, N., 2003. Caledonian orogen, east Greenland 70°–82°N. Geological Map 1:1 000 000. Geological Survey of Denmark and Greenland, Copenhagen.
Henriksen, N., Higgins, A.K., 2008. Geological research and mapping in the caledonian orogen of east Greenland, 70◦N–82◦N, in memoir 202: the Greenland caledonides: evolution of the northeast margin of laurentia. Geol. Soc. Am. 202, 1–27.
Hodell, D.A., Nicholl, J.A., Bontognali, T.R.R., Danino, S., Dorador, J., Dowdeswell, J.A., Röhl, U., 2017. Anatomy of Heinrich layer 1 and its role in the last deglaciation. Paleoceanography 32, 284–303.
Hodell, D.A., Channell, J.E.T., Curtis, J.H., Romero, O.E., Röhl, U., 2008. Onset of "hudson strait" heinrich events in the eastern North Atlantic at the end of the middle pleistocene transition (~640 ka)? Paleoceanography 23.
Hogan, K.A., Jakobsson, M., Mayer, L., Reilly, B.T., Jennings, A.E., Stoner, J.S., Nielsen, T., Andresen, K.J., Nørmark, E., Heirman, K.A., Kamla, E., Jerram, K., Stranne, C., Mix, A., 2020. Glacial sedimentation, fluxes and erosion rates associated with ice retreat in Petermann Fjord and Nares Strait, north-west Greenland. Cryosphere 14, 261–286.
Hogan, K.A., Dowdeswell, J.A., Ó Cofaigh, C., 2012. Glacimarine sedimentary processes and depositional environments in an embayment fed by West Greenland ice streams. Mar. Geol. 311–314, 1–16.
Hogan, K.A., Ó 'Cofaigh, C., Jennings, A.E., Dowdeswell, J.A., Hiemstra, J.F., 2016. Deglaciation of major paleo-ice stream in Disko trough, west Greenland. Quat. Sci. Rev. 147, 5–26.
Hopkins, T.S., 1991. The GIN Sea-A synthesis of its physical oceanography and literature review 1972–1985. Earth Sci. Rev. 30, 175–318.
Hubberten, H.-W., Grobe, H., Jokat, W., Melles, M., Niessen, F., Stein, R., 1995. Glacial history of east Greenland explored. Eos 76 (36), 353–364.
Hulbe, C.L., MacAyeal, D.R., Denton, G.H., Kleman, J., Lowell, T.V., 2004. Catastrophic ice shelf breakup as the source of Heinrich event icebergs. Paleoceanography 19.
Hull, D.M., Osterman, L.E., Thiede, J., 1996. Biostratigraphic synthesis of leg 151, North Atlantic-Arctic gateways. In: Proceedings of the Ocean Drilling Program, Scientific Results, vol. 151. Ocean Drilling Program, College Station, Tex, pp. 627–644.
IPCC, 2021. In: Zhai, P., Pirani, A., Connors, S.L., Péan, C., Berger, S., Caud, N., Chen, Y., Goldfarb, L., Gomis, M.I., Huang, M., Leitzell, K., Lonnoy, E., Matthews, J.B.R., Maycock, T.K., Waterfield, T., Yelekçi, O., Yu, R., Zhou, B. (Eds.).
Jackson, R., Andreasen, N., Oksman, M., Andersen, T.J., Christof Pearce, C., Seidenkrantz, M.-S., Ribeiro, S., 2022. Marine conditions and development of the sirius water polynya on the north-east Greenland shelf during the younger dryas holocene. Quat. Sci. Rev. 291, 107647.
Jakobsson, M., Andreassen, K., Bjarnadóttir, L.R., Dove, D., Dowdeswell, J.A., England, J.H., Funder, S., Hogan, K., Ingólfsson, Ó., Jennings, A., Krog Larsen, N., Kirchner, N., Landvik, J.Y., Mayer, L., Mikkelsen, N., Moller, P., Niessen, F., Nilsson, J., O'Regan, M., Polyak, L., Nørgaard-Pedersen, N., Stein, R., 2014. Arctic Ocean glacial history. Quat. Sci. Rev. 92, 40–67.
Jamieson, S.S.R., Vieli, A., Livingstone, S.J., Ó Cofaigh, C., Stokes, C., Hillenbrand, C.-D., Dowdeswell, J.A., 2012. Ice-stream stability on a reverse bed slope. Nat. Geosci. 5, 799–802.
Jenkins, A., Dutrieux, P., Jacobs, S.S., McPhail, S., Perrett, J.R., Webb, A.T., White, D., 2010. Observations beneath pine island glacier in West Antarctica and implications for its retreat. Nat. Geosci. 3, 468–472.
Jennings, A.E., Andrews, J.T., Reilly, B., Walczak, M., Jakobsson, M., Mix, A., Stoner, J. S., Nicholls, K.W., Cheseby, M., 2020. Modern foraminiferal assemblages in northern Nares Strait, Petermann fjord, and beneath Petermann ice tongue, NW Greenland. Arctic Antarct. Alpine Res. 52 (1), 491–511.
Jennings, A., Reilly, B., Andrews, J., Hogan, K., Walczak, M., Jakobsson, M., Stoner, J., Mix, A., Nicholls, K.W., O'Regan, M., Prins, M.A., 2022. Modern and early holocene

ice shelf sediment facies from Petermann Fjord and northern Nares Strait, northwest Greenland. Quat. Sci. Rev. 283, 107460.
Jennings, A.E., Hald, M., Smith, M., Andrews, J.T., 2006. Freshwater forcing from the Greenland ice sheet during the Younger Dryas: evidence from southeastern Greenland shelf cores. Quat. Sci. Rev. 25, 282–298.
Jennings, A.E., Knudsen, K.L., Hald, M., Hansen, C.V., Andrews, J.T., 2002. A mid-Holocene shift in Arctic sea-ice variability on the East Greenland Shelf. Holocene 12, 49–58.
Johannessen, O.M., 1986. Brief overview of the physical oceanography. In: Hurdle, B.G. (Ed.), The Nordic Seas. Springer, New York, NY, pp. 103–128.
Johnsen, S.J., Dahl-Jensen, D., Gundestrup, N., Steffensen, J.P., Clausen, H.B., Miller, H., Masson-Delmotte, V., Sveinbjörnsdottir, A.E., White, J., 2001. Oxygen isotope and palaeotemperature records from six Greenland ice-core stations: camp Century, Dye-3, GRIP, GISP2, Renland and NorthGRIP. J. Quat. Sci. 16 (4), 299–307.
Joughin, I., Abdalati, W., Fahnestock, M., 2004. Large fluctuations in speed on Greenland's Jakobshavn Isbrae glacier. Nature 432, 608–610.
Joughin, I., Fahnestock, M., MacAyeal, D., Bamber, J.L., Gogineni, P., 2001. Observation and analysis of ice flow in the largest Greenland ice stream. J. Geophys. Res. 106 (D24), 34021–34034.
Joughin, I., Smith, B.E., Howat, I.M., 2018. A complete map of Greenland ice velocity derived from satellite data collected over 20 years. J. Glaciol. 64 (243), 1–11.
Khan, S.A., Kjær, K.H., Bevis, M., Bamber, J.L., Wahr, J., Kjeldsen, K.K., Bjørk, A.A., Korsgaard, N.J., Stearns, L.A., van den Broeke, M.R., Liu, L., Larsen, N.K., Muresan, I. S., 2014. Sustained mass loss of the northeast Greenland ice sheet triggered by regional warming. Nat. Clim. Change 4, 292–299.
Kilfeather, A.A., Ó Cofaigh, C., Lloyd, J.M., Dowdeswell, J.A., Xu, S., Moreton, S.G., 2011. Ice-stream retreat and ice-shelf history in marguerite trough, antarctic peninsula: sedimentological and foraminiferal signatures. GSA Bull. 123 (5/6), 997–1015.
King, E.C., Hindmarsh, R.C., Stokes, C.R., 2009. Formation of mega-scale glacial lineations observed beneath a West Antarctic ice stream. Nat. Geosci. 2 (8), 585–588.
Klages, J.P., Kuhn, G., Hillenbrand, C.-D., Graham, A.G.C., Smith, J.A., Larter, R.D., Gohl, K., 2013. First geomorphological record and glacial history of an inter-ice stream ridge on the West Antarctic continental shelf. Quat. Sci. Rev. 61, 47–61.
Klug, M., Bennike, O., Wagner, B., 2009. Repeated short-term bioproductivity changes in a coastal lake on Store Koldewey, northeast Greenland: an indicator of varying sea-ice coverage? Holocene 19.
Krissek, L.A., 1995. LateCenozoicice-raftingrecordsfromLeg145Sitesinthe north pacific: late Miocene onset, late Pliocene intensification, and pliocene–pleistocene events. In: Rea, D.K., Basov, I.A., Scholl, D.W., Allan, J.F. (Eds.), Proceedings of the Ocean Drilling Program—Scientific Results, vol. 145, pp. 179–194, 1995.
Landvik, J.Y., 1994. The last glaciation of Germania land and adjacent areas, northeast Greenland. J. Quat. Sci. 9, 81–92.
Larsen, N.K., Søndergaard, A.S., Levy, L.B., Strunk, A., Skov, D.S., Bjørk, A., Khan, S.A., Olsen, J., 2022. Late glacial and holocene glaciation history of north and northeast Greenland. Arctic Antarct. Alpine Res. 54, 294–313.
Larsen, N.K., Levy, L.B., Carlson, A.E., Buizert, C., Olsen, J., Strunk, A., Bjork, A.A., Skov, D.S., 2018. Instability of the northeast Greenland ice stream over the last 45,000 years. Nat. Commun. 9, 1872.
Larsen, N.K., Piotrowski, J.A., Kronborg, C., 2004. A Multiproxy Study of a Basal till: a Time-Transgressive Accretion.
Lloyd, J.M., Ribeiro, S., Weckström, K., Callard, L., Cofaigh, C.Ó., Leng, M.J., Gulliver, P., Roberts, D.H., 2023. Ice-ocean interactions at the Northeast Greenland Ice stream (NEGIS) over the past 11,000 years. Quat. Sci. Rev. 308, 108068.
López-Quirós, A., Lobo, F.J., Duffy, M., Leventer, A., Evangelinos, D., Escutia, C., Bohoyo, F., 2021. Late Quaternary high-resolution seismic stratigraphy and core-based paleoenvironmental reconstructions in Ona Basin, southwestern Scotia Sea (Antarctica). Mar. Geol. 439, 106565.
Löwemark, L., März, C., O'Regan, M., Gyllencreutz, R., 2014. Arctic Ocean Mn-stratigraphy: genesis, synthesis and inter-basin correlation. Quat. Sci. Rev. 92, 97–111.
Macdonald, R., Gobeil, C., 2012. Manganese sources and sinks in the arctic ocean with reference to Periodic enrichments in basin sediments. Aquat. Geochem. 1–27.
Madsen, T.M., Piotrowski, J.A., 2012. Genesis of the glaciotectonic thrust-fault complex at Halk Hoved, southern Denmark. Bull. Geol. Soc. Den. 60, 61–80.
Marcott, S.A., Clark, P.U., Padman, L., Klinkhammer, G.P., Springer, S.R., Zhengyu, L., Otto-Bliesner, B., Carlson, A., Ungerer, A., Padman, J., He, F., Cheng, J., Schmittner, A., 2011. Ice shelf collapse from subsurface warming as a trigger for Heinrich events. Proc. Natl. Acad. Sci. USA 108 (33), 13415–13419.
März, C., Stratmann, A., Matthiessen, J., Meinhardt, A.K., Eckert, S., Schnetger, B., Vogt, C., Stein, R., Brumsack, H.J., 2011. Manganese-rich brown layers in Arctic Ocean sediments: composition, formation mechanisms, and diagenetic overprint. Geochem. Cosmochim. Acta 75, 7668–7687.
Mayer, C., Schaffer, J., Hattermann, T., Floricioiu, D., Krieger, L., Dodd, P.A., et al., 2018. Large ice loss variability at Nioghalvfjerdsfjorden glacier, Northeast-Greenland. Nat. Commun. 9 (1), 2768.
Monien, D., Kuhn, G., von Eynatten, H., Talarico, F.M., 2012. Geochemical provenance analysis of fine-grained sediment revealing Late Miocene to recent Paleo-Environmental changes in the Western Ross Sea, Antarctica. Global Planet. Change 96–97, 41–58.
Morlighem, M., Williams, C.N., Rignot, E., An, L., Arndt, J.E., Bamber, J.L., Catania, G., Chauche, N., Dowdeswell, J.A., Dorschel, B., Fenty, I., Hogan, K., Howat, I., Hubbard, A., Jakobsson, M., Jordan, T.M., Kjeldsen, K.K., Millan, R., Mayer, L., Mouginot, J., Noel, B.P.Y., O' Cofaigh, C., Palmer, S., Rysgaard, S., Seroussi, H., Siegert, M.J., Slabon, P., Straneo, F., van den Broeke, M.R., Weinrebe, W., Wood, M., Zinglersen, K.B., 2017. BedMachine v3: complete bed topography and ocean bathymetry mapping of Greenland from multibeam echo sounding combined with mass conservation. Geophys. Res. Lett. 44 (21), 11051–11061.
Mouginot, J., Rignot, E., Scheuchl, B., Fenty, I., Khazendar, A., Morlighem, M., Buzzi, A., Paden, J., 2015. Fast retreat of zachariæ Isstrøm, northeast Greenland. Science 350, 1357–1361.
Müller, J., Werner, K., Stein, R., Fahl, K., Moros, M., Jansen, E., 2012. Holocene cooling culminates in sea ice oscillations in Fram Strait. Quat. Sci. Rev. 47, 1–14.
Newton, A.M.W., Knutz, P.C., Huuse, M., Gannon, P., Brocklehurst, S.H., Clausen, O.R., Gong, Y., 2017. Ice stream reorganization and glacial retreat on the northwest Greenland shelf. Geophys. Res. Lett. 44, 7826–7835.
Nielsen, T., Rasmussen, T.L., 2018. Reconstruction of ice sheet retreat after the Last Glacial maximum in Storfjorden, southern Svalbard. Mar. Geol. 402, 228–243.
Nørgaard-Pedersen, N., Mikkelsen, N., Kristoffersen, Y., 2008. Late glacial and holocene marine records from the independence fjord and Wandel Sea regions, north Greenland. Polar Res. 27, 209–221.
Ó Cofaigh, C., Dowdeswell, J.A., 2001. Laminated sediments in glacimarine environments: diagnostic criteria for their interpretation. Quat. Sci. Rev. 20 (13), 1411–1436.
Ó Cofaigh, C., Dowdeswell, J.A., Allen, C.S., Hiemstra, J.F., Pudsey, C.J., Evans, J., Evans, D.J., 2005. Flow dynamics and till genesis associated with a marine-based Antarctic palaeo-ice stream. Quat. Sci. Rev. 24 (5), 709–740.
Ó Cofaigh, C., Dowdeswell, J.A., Evans, J., Larter, R.D., 2008. Geological constraints on Antarctic palaeo-ice-stream retreat. Earth Surf. Process. Landforms 33 (4), 513–525.
Ó Cofaigh, C., Dowdeswell, J.A., Kenyon, N.H., Evans, J., Taylor, J., Mienert, J., Wilken, M., 2004. Timing and significance of glacially-influenced mass wasting in the submarine channels of the Greenland Basin. Mar. Geol. 207, 39–54.
Ó Cofaigh, C., Evans, J., Dowdeswell, J.A., Larter, R.D., 2007. Till characteristics, genesis and transport beneath Antarctic paleo-ice streams. J. Geophys. Res. Earth Surf. 112 (F3).
Ó Cofaigh, C., Stokes, C.R., 2008. Reconstructing ice-sheet dynamics from subglacial sediments and landforms: introduction and overview. Earth Surf. Process. Landforms 33, 495–502.
Olsen, I.L., Rydningen, T.A., Forwick, M., Laberg, J.S., Husum, K., 2020. Last glacial ice sheet dynamics offshore NE Greenland – a case study from store Koldewey trough. Cryosphere 14, 4475–4494.
Ottesen, D., Dowdeswell, J.A., 2009. An inter-ice-stream glaciated margin: submarine landforms and a geomorphic model based on marine-geophysical data from Svalbard. Geol. Soc. Am. Bull. 121 (11/12), 1647–1665.
Ottesen, D., Dowdeswell, J.A., Landvik, J., Mienert, J., 2007. Dynamics and retreat of the Late Weichselian ice sheet on Svalbard inferred from high-resolution sea-floor morphology. Boreas 36, 286–306.
Pados-Dibattista, T., Pearce, C., Detlef, H., Bendtsen, J., Seidenkrantz, M.-S., 2022. Holocene palaeoceanography of the Northeast Greenland shelf. Clim. Past 18, 103–127.
Paytan, A., Griffith, E.M., 2007. Marine barite: recorder of variations in ocean export productivity. Deep-Sea Res. II 54, 687–705.
Petersen, T.G., 2021. New sequence stratigraphic framework on a 'passive' margin: implications for the post-break-up depositional environment and onset of glaciomarine conditions in NE Greenland. J. Geol. Soc. 178 (2), 1–18.
Piotrowski, J.A., Larsen, N.K., Menzies, J., Wysota, W., 2006. Formation of subglacial till under transient bed conditions: deposition, deformation, and basal decoupling under a Weichselian ice sheet lobe, central Poland. Sedimentology 53, 83–106.
Polyak, L., Korsun, S., Febo, L.A., Stanovoy, V., Khusid, T., Hald, M., Paulsen, B.E., Lubinski, D.J., 2002. Benthic foraminiferal assemblages from the southern Kara Sea, a river-influenced Arctic marine environment. J. Foraminifer. Res. 32, 252–273.
Prothro, L.O., Simkins, L.M., Majewski, W., Anderson, J.B., 2018. Glacial retreat patterns and processes determined from integrated sedimentology and geomorphology records. Mar. Geol. 395, 104–119.
Pudsey, C.L., Murray, J.W., Appleby, P., Evans, J., 2006. Ice shelf history from petrographic and foraminiferal evidence, Northeast Antarctic Peninsula. Quat. Sci. Rev. 25, 2357–2379.
Quadfasel, D., Rudels, B., Kurtz, K., 1988. Outflow of dense water from a svalbard fjord into the Fram Strait. Deep-Sea Res., Part A 35, 1143–1150.
Rasmussen, T.L., Pearce, C., Andresen, K.J., Nielsen, T., Seidenkrantz, M.-S., 2022. Northeast Greenland: ice-free shelf edge at 79.4°N around the Last Glacial Maximum 25.5–17.5 ka. Boreas 51 (4), 759–775.
Rasmussen, T.L., Thomsen, E., 2004. The role of the North Atlantic Drift in the millennial timescale glacial climate fluctuations. Palaeogeogr. Palaeoclimatol. Palaeoecol. 210, 101–116.
Rasmussen, T.L., Thomsen, E., 2021. Climate and ocean forcing of ice-sheet dynamics along the Svalbard-Barents Sea Ice Sheet during the deglaciation 20,000–10,000 years BP. Quaternary Sci. Adv. 3, 100019.
Rasmussen, T.L., Thomsen, E., Ślubowska, M.A., Jessen, S., Solheim, A., Koç, N., 2007. Paleoceanographic evolution of the SW Svalbard margin (76°N) since 20,000 14C yr BP. Quat. Res. 67, 100–114.
Rebesco, M., Liu, Y., Camerlenghi, A., Winsborrow, M., Laberg, J.S., Caburlotto, A., Tomini, I., 2011. Deglaciation of the western margin of the Barents Sea Ice Sheet - a swath bathymetric and sub-bottom seismic study from the Kveithola Trough. Mar. Geol. 279 (1–4), 141–147.
Reeh, N., Thomsen, H.H., Higgins, A.K., Weidick, A., 2001. Sea ice and the stability of north and Northeast Greenland floating glaciers. Ann. Glaciol. 33, 474–480.
Reilly, B.T., Stoner, J.S., Wiest, J., 2017. Sed CT: MATLABTM tools for standardized and quantitative processing of sediment core computed tomography (CT) data collected using a medical CT scanner. G-cubed 18 (8), 3231–3240.
Reilly, B.T., Stoner, J.S., Mix, A.C., Walczak, M.H., Jennings, A.E., Jakobsson, M., Dyke, L., Glueder, A., Nicholls, K., Hogan, K.A., Mayer, L.A., Hatfield, R.G.,

Albert, S., Marcott, S., Fallon, S., Cheseby, M., 2019. Holocene break-up and reestablishment of the Petermann ice tongue, northwest Greenland. Quat. Sci. Rev. 218, 322e342.
Reimer, P.J., Reimer, R.W., 2001. A marine reservoir correction database and on-line interface. Radiocarbon 43 (2A), 461–463.
Richter, T.O., van der Gaast, S., Koster, B., Vaars, A., Gieles, R., Stigter, H.C., de Haas, H. D., van Weering, van, T.C.E., 2006. The Avaatech XRF Core Scanner: technical description and applications to NE Atlantic sediments. Geol. Soc. Lond. Spec. Publ. 267, 39–50.
Roberts, D.H., Rea, B.R., Lane, T.P., Schnabel, C., Rodés, A., 2013. New constraints on Greenland ice sheet dynamics during the last glacial cycle: evidence from the Uummannaq ice stream system. J. Geophys. Res. 118, 519–541.
Rogerson, M., Rohling, E.J., Weaver, P.P.E., 2006. Promotion of meridional overturning by Mediterranean-derived salt during the last deglaciation. Paleoceanography 21, PA4101.
Röhl, U., Westerhold, T., Bralower, T.J., Zachos, J.C., 2007. On the duration of the paleocene-eocene thermal maximum (PETM). G-cubed 8, Q12002.
Rothwell, R.G., Croudace, I.W., 2015. Twenty years of XRF core scanning marine sediments: what do geochemical proxies tell us? In: Croudace, I.W., Rothwell, R.G. (Eds.), Micro-XRF Studies of Sediment Cores. Developments in Paleoenvironmental Research. Springer Science + Business Media, Dordrecht, pp. 25–101.
Rudels, B., Björk, G., Nilsson, J., Winsor, P., Lake, I., Nohr, C., 2005. The interaction between waters from the Arctic Ocean and the nordic seas north of Fram Strait and along the east Greenland current: results from the Arctic Ocean-02 oden expedition. J. Mar. Syst. 55, 1–30.
Rueden, C.T., Schindelin, J., Hiner, M.C., DeZonia, B.E., Walter, A.E., Arena, E.T., Eliceiri, K.W., 2017. ImageJ2: ImageJ for the next generation of scientific image data. BMC Bioinf. 18, 529.
Rydningen, T.A., Vorren, T.O., Laberg, J.S., Kolstad, V., 2013. The marine-based NW Fennoscandian ice sheet: glacial and deglacial dynamics as reconstructed from submarine landforms. Quat. Sci. Rev. 68, 126–141.
Sáez, A., Valero-Garcés, B.L., Giralt, S., Moreno, A., Bao, R., Pueyo, J.J., Hernández, A., Casas, D., 2009. Glacial to holocene climate changes in the SE pacific. The raraku lake sedimentary record (easter Island, 27°S). Quat. Sci. Rev. 28, 2743–2759.
Salabarnada, A., Escutia, C., Röhl, U., Nelson, C.H., McKay, R., Jiménez-Espejo, F.J., Bijl, P.K., Hartman, J.D., Strother, S.L., Salzmann, U., Evangelinos, D., López-Quirós, A., Flores, J.A., Sangiorgi, F., Ikehara, M., Brinkhuis, H., 2018. Paleoceanography and ice sheet variability offshore Wilkes Land, Antarctica – part 1: insights from late Oligocene astronomically paced contourite sedimentation. Clim. Past 14, 991–1014.
Schaffer, J., von Appen, W.J., Dodd, P.A., Hofstede, C., Mayer, C., de Steur, L., Kanzow, T., 2017. Warm water pathways toward nioghalvfjerdsfjorden glacier, northeast Greenland. J. Geophys. Res. Ocean. 122, 4004–4020.
Schoof, C., 2007. Ice sheet grounding line dynamics: steady states, stability, and hysteresis. J. Geophys. Res. 112 (F3).
Seidenkrantz, M.-S., 1995. *Cassidulina teretis* Tappan and *Cassidulina neoteretis* new species (Foraminifera): stratigraphic markers for deep sea and outer shelf areas. J. Micropalaeontol. 14, 145–157.
Seidenkrantz, M.-S., Andersen, J.R., Andresen, K.J., Bendtsten, J., Brice, C., Ellegaard, M., Eriksen, L.N., Gariboldi, K., Le Duc, C., Mathiasen, A.M., Nielsen, T., Ofstad, S., Pearce, C., Rasmussen, T.L., Ribeiro, S., Rysgaard, S., Røy, H., Scholze, C., Schultz, M., Wangner, D.J., 2018. NorthGreen2017 - a marine research expedition to NE Greenland onboard 'R/V Dana. Cruise Report.
Shepherd, A., et al., 2012. A reconciled estimate of ice-sheet mass balance. Science 338, 1183–1189.
Slubowska-Woldengen, M., Rasmussen, T.L., Koç, N., Klitgaard-Kristensen, D., Nilsen, F., Solheim, A., 2007. Advection of atlantic water to the western and northern svalbard shelf since 17,500calyr BP. Quat. Sci. Rev. 26, 463–478.
Smith, J.A., Andersen, T.J., Shortt, M., Gaffney, A.M., Truffer, M., Stanton, T.P., Bindschadler, R., Dutrieux, P., Jenkins, A., Hillenbrand, C.D., Ehrmann, W., Corr, H. F.J., Farley, N., Crowhurst, S., Vaughan, D.G., 2017. Sub-ice-shelf sediments record history of twentieth-century retreat of Pine Island Glacier. Nature 541, 77–80.
Smith, J.A., Graham, A.G.C., Post, A.L., Hillenbrand, C.D., Bart, P.J., Powell, R.D., 2019. The marine geological imprint of Antarctic ice shelves. Nat. Commun. 10, 5635.
Smith, J.A., Callard, L., Bentley, M.J., Jamieson, S.S.R., Sanchez-Montes, M.L., Lane, T. P., Lloyd, J.M., McClymont, E.L., Darvill, C.M., Rea, B.R., O'Cofaigh, C., Gulliver, P., Ehrmann, W., Jones, R.S., Roberts, D.H., 2023. Holocene history of 79°N ice shelf reconstructed from epishelf lake and uplifted glacimarine sediments. Cryosphere 17, 1247–1270.
Smith, J.A., Hillenbrand, C.-D., Kuhn, G., Larter, R.D., Graham, A.G.C., Ehrmann, W., Moreton, S.G., Forwick, M., 2011. Deglacial history of the west antarctic ice sheet in the western Amundsen Sea embayment. Quat. Sci. Rev. 30, 488–505.
Spagnolo, M., Clark, C.D., Ely, J.C., Stokes, C.R., Anderson, J.B., Andreassen, K., Graham, A.G.C., King, E.C., 2014. Size, shape and spatial arrangement of mega-scale glacial lineations from a large and diverse dataset. Earth Surf. Process. Landforms 39, 1432–1448.
Spielhagen, R.F., Mackensen, A., 2021. Upper ocean variability off NE Greenland (79N) since the last glacial maximum reconstructed from stable isotopes in planktic foraminifer morphotypes. Quat. Sci. Rev. 265, 107070.
Stein, R., 2008. Chapter six quaternary variability of palaeoenvironment and its sedimentary record. In: Stein, R.B.T., M, G.D. (Eds.), Developments in Marine Geology. Elsevier, pp. 287–437.
Stein, R., Fahl, K., Schreck, M., Knorr, G., Niessen, F., Forwick, M., et al., 2016. Evidence for ice-free summers in the late Miocene central Arctic Ocean. Nat. Commun. 7, 11148.
Stein, R., Nam, S. Il, Grobe, H., Hubberten, H., 1996. Late Quaternary glacial history and short-term ice-rafted debris fluctuations along the East Greenland continental margin. Geol. Soc. Spec. Publ. 111, 135–151.
Stewart, F.S., Stoker, M.S., 1990. Problems associated with seismic facies analysis of diamicton-dominated, shelf glacigenic sequences. Geo Mar. Lett. 10, 151–156.
Straneo, F., Heimbach, P., 2013. North Atlantic warming and the retreat of Greenland's outlet glaciers. Nature 504, 36–43.
Streuff, K., Ó Cofaigh, C., Hogan, K., Jennings, A., Lloyd, J.M., Noormets, R., Nielsen, T., Kuijpers, A., Dowdeswell, J.A., Weinrebe, W., 2017. Seafloor geomorphology and glacimarine sedimentation associated with fast-flowing ice sheet outlet glaciers in Disko Bay, West Greenland. Quat. Sci. Rev. 169, 206–230.
Streuff, K., Ó Cofaigh, C., Noormets, R., Lloyd, J., 2018. Submarine landform assemblages and sedimentary processes in front of Spitsbergen tidewater glaciers. Mar. Geol. 402, 209–227.
Stuiver, M., Reimer, P.J., Reimer, R.W., 2021. Calib 8.2 [WWW program] at J. Quat. Sci. 19, 9–21. http://calib.org. (Accessed 1 July 2022). and deformation hypothesis.
Syring, N., Lloyd, J.M., Stein, R., Fahl, K., Roberts, D.H., Callard, L., O' Cofaigh, C., 2020. Holocene interactions between glacier retreat, sea-ice formation and Atlantic Water advection at the inner Northeast Greenland continental shelf. Paleoceanogr. Paleoclimatol. 35, e2020PA004019.
Talling, P.J., Masson, D.G., Sumner, E.J., Melgesini, G., 2012. Subaqeous sediment density flows: depositional processes and deposit types. Sedimentology 59, 1937–2003.
The IMBIE Team, 2020. Mass balance of the Greenland ice sheet from 1992 to 2018. Nature 579, 233–239.
Tucker, M.E., 2001. Sedimentary Petrology: an Introduction to the Origin of Sedimentary Rocks. Blackwell Science Ltd., Oxford, p. 260.
van den Broeke, M.R., Enderlin, E.M., Howat, I.M., Munneke, P.K., Noël, B.P.Y., van den Berg, W.J., van Meijgaard, E., Wouters, B., 2016. On the recent contribution of the Greenland ice sheet to sea level change. Cryosphere 10, 1933. –1946.
Vinther, B.M., Buchardt, S.L., Clausen, H.B., Dahl-Jensen, D., Johnsen, S.J., Fisher, D.A., Koerner, R.M., Raynaud, D., Lipenkov, V., Andersen, K.K., Blunier, T., 2009. Holocene thinning of the Greenland ice sheet. Nature 461, 385–388.
Wacker, L., Fahrni, S.M., Hajdas, I., Molnar, M., Synal, H.-A., Szidat, S., Zhang, Y.L., 2013a. A versatile gas interface for routine radiocarbon analysis with a gas ion source. Nucl. Instrum. Methods Phys. Res. Sect. B Beam Interact. Mater. Atoms 294, 315–319.
Wacker, L., Lippold, J., Molnar, M., Schulz, H., 2013b. Towards radiocarbon dating of single foraminifera with a gas ion source. Nucl. Instrum. Methods Phys. Res. Sect. B Beam Interact. Mater. Atoms 294, 307–310.
Weltje, G.J., Tjallingii, R., 2008. Calibration of XRF core scanners for quantitative geochemical logging of sediment cores: theory and application. Earth Planet Sci. Lett. 274, 423–438.
Werner, K., Müller, J., Husum, K., Spielhagen, R.F., Kandiano, E.S., Polyak, L., 2016. Holocene sea subsurface and surface water masses in the Fram Strait e comparisons of temperature and sea-ice reconstructions. Quat. Sci. Rev. 147, 194–209.
Willcox, E.W., Bendtsen, J.B., Mortensen, J., Mohn, C., Lemes, M., Pedersen, T.J., Holding, J.J., Møller, E.F., Sejr, M.K., Seidenkrantz, M.-S., Rysgaard, S., 2023. An updated view on water masses on the Northeast Greenland shelf and their link to the Laptev Sea and Lena River. J. Geophys. Res., Oceans 128 (4).
Wilson, N.J., Straneo, F., 2015. Water exchange between the continental shelf and the cavity beneath nioghalvfjerdsbræ (79 north glacier). Geophysical research letters. Geophys. Res. Lett. 42, 7648–7654.
Winkelmann, D., Jokat, W., Jensen, L., Schenke, H.-W., 2010. Submarine end moraines on the continental shelf off NE Greenland e implications for Late glacial dynamics. Quat. Sci. Rev. 29, 1069–1077.
Wolters, S., Zeller, M., Bungenstock, F., 2010. Early Holocene environmental history of sunken landscapes: pollen, plant macrofossil and geochemical analyses from the Borkum Riffgrund, southern North Sea. Int. J. Earth Sci. 99, 1707–1719.
Wood, M., Rignot, E., Fenty, I., An, L., Bjork, A., van den Broeke, M., et al., 2021. Ocean forcing drives glacier retreat in Greenland. Sci. Adv. 7 (1).
Yokohama, Y., Anderson, J.B., Yamane, M., Simkins, L.M., Miyairi, Y., Yamazaki, T., Koizumi, M., Suga, H., Kusahara, K., Prothro, L., Hasumi, H., Southon, R., Ohkouchi, N., 2016. Widespread collapse of the ross ice shelf during the late holocene. Proc. Natl. Acad. Sci. USA 113 (9), 2354–2359.
Zaragosi, S., Bourillet, J.-F., Eynaud, F., Toucanne, S., Denhard, B., Van Toer, A., Lanfumey, V., 2006. The impact of the last European deglaciation on the deep-sea turbidite systems of the Celtic-Armorican margin (Bay of Biscay). Geo Mar. Lett. 26, 17–329.
Ziegler, M., Lourens, L.J., Tuenter, E., Reichart, G.-J., 2010. High Arabian Sea productivity conditions during MIS 13 – odd monsoon event or intensified overturning circulation at the end of the Mid-Pleistocene transition? Clim. Past 6, 63–76.